

12-2008

Finite Element Analysis of Carbon Fiber Composite Ripping Using ABAQUS

Joy Pederson

Clemson University, ppjoy@clemson.edu

Follow this and additional works at: http://tigerprints.clemson.edu/all_theses



Part of the [Engineering Mechanics Commons](#)

Recommended Citation

Pederson, Joy, "Finite Element Analysis of Carbon Fiber Composite Ripping Using ABAQUS" (2008). *All Theses*. Paper 512.

This Thesis is brought to you for free and open access by the Theses at TigerPrints. It has been accepted for inclusion in All Theses by an authorized administrator of TigerPrints. For more information, please contact awesole@clemson.edu.

FINITE ELEMENT ANALYSIS OF CARBON FIBER
COMPOSITE RIPPING USING ABAQUS

A Thesis
Presented to
the Graduate School of
Clemson University

In Partial Fulfillment
of the Requirements for the Degree
Master of Science
Mechanical Engineering

by
Joy Pederson
December 2006

Accepted by:
Dr. Sherrill Biggers, Committee Chair
Dr. John Kennedy
Dr. E. Harry Law

ABSTRACT

An energy dissipation system is proposed for use on consumer passenger automotive vehicles and auto racing stock cars. This system will be utilized to protect the occupants from frontal impacts with stationary or near stationary objects. The system will be affixed to the front of the car's primary structure. It is proposed to replace the traditional steel bumper currently in use. This system will not increase the weight of the car, nor will it adversely affect the aerodynamics of the body. The system will improve the crashworthiness of the vehicle. Advanced composites will be the primary sacrificial element in the system. Carbon fiber composites are proposed for constructing the system and as the sacrificial element in the system. The system will employ a set of ripping blades to dissipate the energy from an impact and control the deceleration of the vehicle and occupant. A more detailed design explanation can be found in Appendix B. However, the system may be constructed of both steel and composites. The use of composites for the system should significantly lighten the front end of the car and allow greater flexibility in the weight distribution of the vehicle. The proposed system will also be easily modified for different platforms or race conditions and easily replaced in the event of an impact.

Previously, composites have been examined for a similar application. The most prevalent of these designs was the "Humpy bumper," which was composed of multiple layers of carbon fiber which were crushed, and/or delaminated during impact. While this design was prototyped and tested, it was never placed in production. Possibly, one of the largest flaws in the design was that it could only be used once and that the front of the vehicle roll cage might need large modifications.

This thesis will examine the mechanism using ABAQUS to create an accurate model of the material behavior to aid in the design and fine tuning of the ripped assembly before prototyping. This is important because it not only decreases design costs but also the time to market release for the mechanism.

In order to obtain an accurate model, material types and other design variables were investigated. Various material orientations and stacking sequences were explored. Multiple ripper blade profiles were also tested. It was determined that a round ripper blade with a $[+60/-60]_{2S}$ stacking sequence produced the best combination of smooth response with low force.

DEDICATION

I would like to dedicate this thesis to those people who have supported me through all the events that took place to bring it into existence: my parents, without whom I would never have made it this far; and Bryan Craigo and Bill Gibson, without whose encouragement I would never have been able to finish this. It's been a long road with many hills but none too steep to climb.

ACKNOWLEDGMENTS

I would like to thank Dr. Kennedy for all his assistance and believing that this would actually happen. Some days even I wasn't sure I'd finish. I would also like to thank Dr. Law for all the support he has given as I have reached for the stars. Finally, I would like to thank Dr. Biggers and Dr. Summers for their guidance through the maze that is ABAQUS. I never would have had the confidence to tackle this without their support and assistance.

TABLE OF CONTENTS

	Page
TITLE PAGE	i
ABSTRACT	ii
DEDICATION	iv
ACKNOWLEDGEMENTS	v
LIST OF TABLES	viii
LIST OF FIGURES	ix
 CHAPTER	
I. INTRODUCTION	1
II. MECHANICAL PROPERTIES AND PHYSICAL BASIS.....	7
The Ripper	8
The Plate.....	10
Friction.....	13
III. MODEL CREATION	15
Mesh Development.....	15
Material Modeling	19
Contact Interaction Modeling	24
Damage and Failure	25
Hashin’s Failure Theory	25
Element Failure.....	27
IV. RESULTS AND DISCUSSION.....	28
V. CONCLUSIONS.....	47
APPENDICES.....	50
A: ABAQUS VUMAT	51
B: POTENTIAL APPLICATION.....	62

Table of Contents (Continued)

	Page
REFERENCES.....	67

LIST OF TABLES

Table	Page
2.1 Carbon Fiber/PEEK Material Properties	11
2.2 Carbon Epoxy Material Properties	12
3.1 Ply Orientations	16
5.1 Mechanism Energy Absorption	47
5.2 Mechanism Energy Absorption at 0.16 sec	47
5.3 Mechanism Response Curve Smoothness	48

LIST OF FIGURES

Figure	Page
1.1 Tony Stewart's car airborne at Daytona in 2001.....	3
1.2 Ryan Newman at Talladega in April 2003	3
1.3 Albritton Mechanism	4
2.1 Complete ABAQUS Model.....	8
2.2 Ripper Blade	9
2.3 Plate Boundary Conditions	13
2.4 Friction Verification	14
3.1 Mesh Density Case Energy Comparison.....	17
3.2 Energy Comparison for Mesh Densities 0.040, 0.030, and 0.025.....	18
3.3 Energy Comparison for Mesh Densities 0.025 and 0.023.....	19
3.4 Explicit Central-Difference Time Integration.....	23
4.1 Complete Results Graph.....	29
4.2 Element Failure on Plate.....	30
4.3 Element Failure on Zero-Degree Ply.....	30
4.4 Element Failure on +45-Degree Ply.....	31
4.5 Stress Contour at $1.0E^{-2}s$	31
4.6 Stress Contour at $1.5E^{-2}s$	31
4.7 Stress Contour at $2.5E^{-2}s$	32
4.8 Stress Contour at $3.0E^{-2}s$	32

List of Figures (Continued)

Figure	Page
4.9 Stress Contour at $4.0E^{-2}s$	32
4.10 Stress Contour at $5.0E^{-2}s$	32
4.11 Stress Contour at $5.5E^{-2}s$	32
4.12 Stress Contour at $6.0E^{-2}s$	32
4.13 Stress Contour at $7.0E^{-2}s$	33
4.14 Stress Contour at $8.0E^{-2}s$	33
4.15 Stress Contour at $9.5E^{-2}s$	33
4.16 Stress Contour at 0.1050s	33
4.17 Stress Contour at 0.1100s	33
4.18 Stress Contour at 0.1400s	33
4.19 Stress Contour at 0.1450s	34
4.20 Stress Contour at 0.1500s	34
4.21 Stress Contour at 0.1550s	34
4.22 Stress Contour at 0.1650s	34
4.23 Stress Contour at 0.1700s	34
4.24 Stress Contour at 0.1750s	34
4.25 Stress Contour at 0.1800s	35
4.26 Stress Contour at 0.1900s	35
4.27 Stress Contour at 0.1950s	35
4.28 Stress Contour at 0.2000s	35

List of Figures (Continued)

Figure	Page
4.29 Carbon Epoxy Reaction Force.....	36
4.30 Carbon Fiber/PEEK Reaction Force.....	36
4.31 Rounded Ripper Reaction Force.....	37
4.32 Sharp Ripper Reaction Force.....	37
4.33 Blunt Ripper Reaction Force.....	37
4.34 $[0/90]_{2S}$ Reaction Force.....	38
4.35 $[0/90]_{2S}$ Reaction Force Zoom In.....	38
4.36 $[0/90]_{2S}$ Overall View at .075s	39
4.37 $[0/90]_{2S}$ Overall View at .080s	39
4.38 $[0/90]_{2S}$ Overall View at .085s	39
4.39 $[0/90]_{2S}$ Layer 1 View at .075s	40
4.40 $[0/90]_{2S}$ Layer 1 View at .080s	40
4.41 $[0/90]_{2S}$ Layer 1 View at .085s	40
4.42 $[0/90]_{2S}$ Layer 2 View at .075s	41
4.43 $[0/90]_{2S}$ Layer 2 View at .080s	41
4.44 $[0/90]_{2S}$ Layer 2 View at .085s	41
4.45 $[0/90]_{2S}$ Layer 3 View at .075s	42
4.46 $[0/90]_{2S}$ Layer 3 View at .080s	42
4.47 $[0/90]_{2S}$ Layer 3 View at .085s	42
4.48 $[0/90]_{2S}$ Layer 4 View at .075s	43

List of Figures (Continued)

Figure	Page
4.49 [0/90] _{2S} Layer 4 View at .080s	43
4.50 [0/90] _{2S} Layer 4 View at .085s	43
4.51 [+60/-60] _{2S} Reaction Force	44
4.52 [-45/0/+45/0] _S Reaction Force.....	44
4.53 [+30/-30] _{2S} Reaction Force	44
4.54 [-45/0/+45/90] _S Reaction Force	44
4.55 [-45/0/+45/90] _S Thick Reaction Force	45
4.56 [-45/0/+45/90] _{3S} Reaction Force	45
4.57 Plane Stress Model Reaction Force	46
4.58 3D Model Reaction Force.....	46
B-1 Full Mechanism Assembly	63
B-2 Ripping Assembly.....	64
B-3 Ripping Blade with Guide Cone	64
B-4 Ripping Blade without Guide Cone.....	64
B-5 Bumper Designs	65
B-6 Guide Tube Alternatives	66

CHAPTER ONE

INTRODUCTION

Since 2000, stock car racing has lost drivers in its most elite series. The sport lost Dale Earnhardt, Sr., one of its champions, to a multiple car collision with the track exterior wall¹ while both Kenny Irwin and Adam Petty were killed in single car collisions with the outside wall in New Hampshire when vehicle throttles were stuck open². These deaths have led the National Association for Stock Car Auto Racing, or NASCAR, to improve the features in the vehicles and at the tracks in order to prevent additional losses. Some of these improvements include changes or additions to driver equipment, car devices and features, and track structure. Officials have had Steel and Foam Energy Reduction, or SAFER, barriers installed on many of the sport's larger tracks, such as Daytona and Talladega, and required the use of the Head and Neck Support device, or HANS, roof flaps, a roof hatch, and black boxes in the vehicles. These improvements are attempts to reduce the severity of the injuries received by the drivers involved in on-track incidents.

SAFER barriers, also called soft walls, have been added to all high-speed oval tracks³. These barriers are constructed of "3/16 of an inch thick steel tubing, 28 feet long and 8 inches by 8 inches in diameter, backed with thick, closed-cell foam block"³ and have been added to the existing barriers at the track. To prevent secondary collisions, cars are now required to slow to caution speed immediately, instead of the previous practice of finishing the current lap. The HANS device is required by NASCAR for the prevention of possible head-and-neck injuries. More specifically, it aims to prevent a basal skull fracture due to a hyperextended neck, determined to be the cause of death for Dale Earnhardt, Sr., in the

2001 Daytona 500⁴. Standards for racing helmets have also been raised, including the requirement for full-faced helmets.

Vehicles are now required to incorporate roof flaps, roof hatches, and larger windows. Roof flaps are designed to rise when the air flow is reduced by a change in vehicle direction, thus increasing the magnitude of the drag and down forces on the vehicle in an attempt to both keep the vehicle from becoming airborne and to decelerate it⁵. Roof hatches and larger windows have been installed to provide drivers with two unconstrained exits. Also required are black boxes similar to those required in aviation applications. These boxes allow safety experts to learn from the improvements already made and find the places where improvements are still needed. Having active black boxes in all vehicles allows for data collection during on-track incidents that are unexpected or not testable with such current technology as airborne vehicles in varying flight paths, positions and landings, as exemplified in Figure 1.1 below, as well as debris complications, such as the rear axle as shown in Figure 1.2.



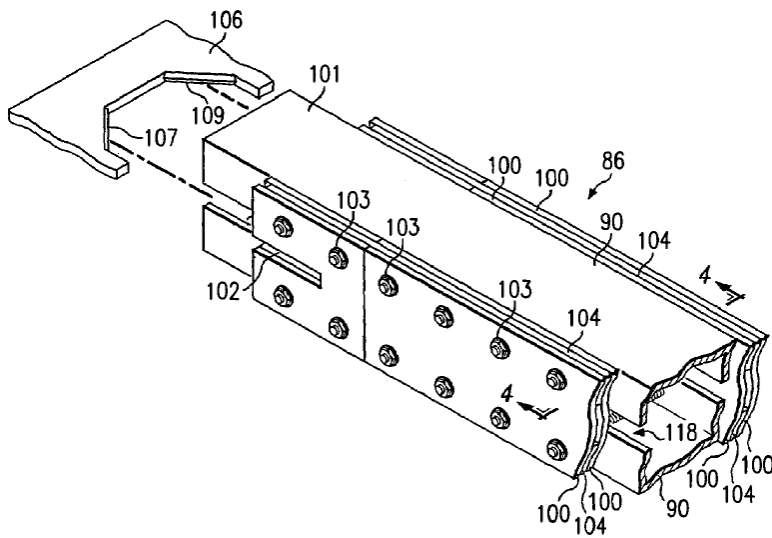
Figure 1.1: Tony Stewart's car airborne at Daytona in 2001⁶



Figure 1.2: Ryan Newman at Talladega in April 2003⁷

While these new requirements have reduced the probability of serious injury, there are still improvements that can be done. One other focus point on the vehicle has been the front bumper. One attempt has already been made to absorb energy in crash situations using this component. The Humpy Bumper, made of carbon-fiber composite, was patented

and track-tested by Lew Composites. However, NASCAR has requested more testing and analysis of this bumper⁸, which included crushing as the energy absorption method. In his examination of the crushing characteristics of carbon fiber composites, Gary Farley has focused on composite tubes and the energy absorption, specifically their shapes and sizes⁹, in relation to their energy absorption capabilities at various crushing speeds¹⁰.



Albritton also proposed using a similar ripping mechanism mounted to the rear of stationary service vehicles used in road way projects¹². Such a device is designed to reduce the magnitude of the impact the parked vehicle experiences when rear-ended by a vehicle moving on the roadway. By lowering the impact height, the chance of a vehicle under-run incident, i.e. one in which a smaller vehicle runs underneath the rear of a larger vehicle, is also reduced. These incidents can be quite severe as smaller vehicles are not designed to take impacts across the windshield.

It has long been known that carbon fiber composites can be substituted for traditional structural materials such as steel and aluminum. This material substitution can save weight and/or size or improve some measure of performance depending on the application. The use of well designed composites can also reduce manufacturing time and/or cost by requiring less processing and fewer parts. Currently, Boeing is incorporating significant quantities of carbon fiber in the new 7E7 Dreamliner¹³. In the case of Boeing, carbon fiber is substituted for aluminum allowing for a stronger fuselage structure in the aircraft design to reduce jet lag by keeping cabin pressure closer to that of sea level than the standard cabin pressure.¹⁴ Boeing has also constructed the wings and tail section from carbon fiber composite.¹⁵

For this project, the energy absorption capabilities of a laminated composite plate by ripping will be examined. The application involves a sacrificial link between the bumper of a modern stock car or production vehicle and the frame and, ultimately, the driver and/or passenger(s) in the vehicle. Given appropriate data and testing, the design of the ripping device could be optimized or tuned for specific applications without significant modifications to either the device or the vehicle. Tuning allows for a device stiff enough to

withstand “bump and rub” racing without damage but still soft and tough enough to absorb wreck-related impacts. The ply orientations, ripper shape, and plate material will be varied to determine their effect. Interlaminar effects will also be studied to determine the extent to which they contribute to material failure and the energy absorption performance of the device.

CHAPTER TWO

MECHANICAL PROPERTIES AND PHYSICAL BASIS

A finite element analysis was utilized to model accurately a composite laminate plate and its lamina. The model itself consists of two components: the ripper and the plate. The composite laminate was constructed using ABAQUS¹⁶ so that when the plate stood on edge, the plies were oriented in the 1-2 plane as shown in Figure 2.1. All plies were modeled as linear elastic orthotropic materials. The ripper was rigid and moved at a low velocity. The model was used to examine the effects of laminate orientation and stacking, ripper shape, and two different materials. Figure 2.1, below, shows the entire model in ABAQUS.

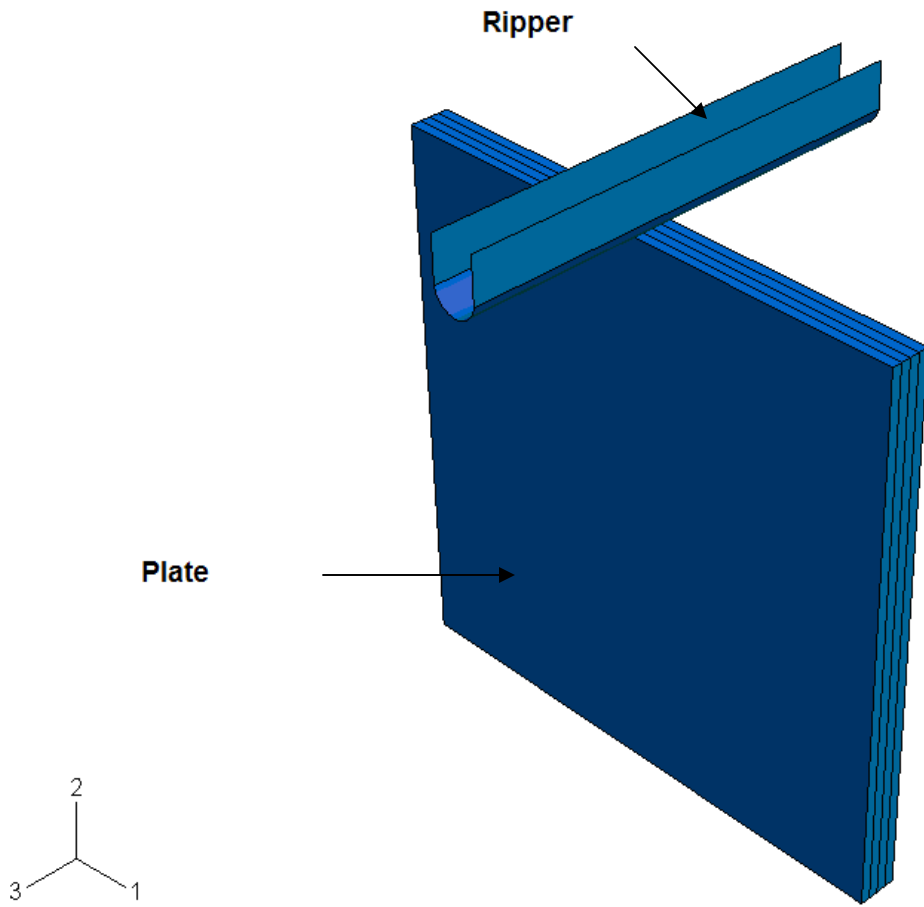


Figure 2.1: Complete ABAQUS Model

The Ripper

The ripper was modeled as a 3D analytically rigid part, one of three options for 3D part design in ABAQUS, the other two being deformable and discrete rigid. While discrete rigid parts have greater geometric flexibility, an analytically rigid part was created in this study because surfaces can be defined as straight and curved line segments, which is computationally cheaper in contact models¹⁷. The part itself is an extruded cross-section of 1 inch height and 0.0633 inch width shown below in Figure 2.2, with the rounded leading edge shown in orange and with the blunt and sharp leading edge designs overlaid in black. The

rounded leading edge of the design shown was chosen for simplicity as compared to the other shapes modeled. Its reference point was specified at the center of mass.

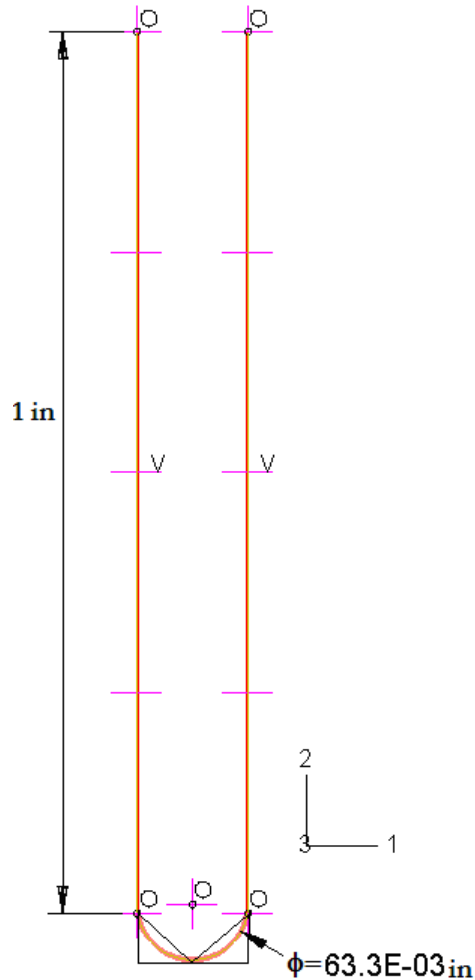


Figure 2.2: Ripper Blade

The ripper blade is constrained to translate only in the 2-direction. In addition, a constant velocity of 5 inches per second has been specified as the velocity of the ripper as it moves into the plate. This value was chosen to simulate a quasistatic response for the mechanism. A quasistatic state was chosen to simplify the model by eliminating the impact

event so that the mechanism effectiveness could be evaluated and possible material options chosen without large computation times.

The Plate

The composite plate, a square of dimensions 3 inches, was composed of carbon fiber/PEEK with approximately 30% resin. The required material properties for 3D analysis are listed in Table 2.1. The plies were assumed to be transversely isotropic in nature. G_{23} was calculated using information and equations found in Downs¹⁸, while Poisson's ratio for the 2-3 plane came from Carlile¹⁹, and matrix direction compressive strengths from Klett²⁰. Since no reliable source was found for S_{23} , the value used was based on the ratio of "typical" material property values provided by ABAQUS to S_{23} .

Table 2.1: Carbon Fiber/ PEEK Material Mechanical Properties

E_{11}^*	Young's modulus along fiber direction 1 (psi)	2.16E+07
E_{22}^*	Young's modulus along matrix direction 2 (psi)	1.28E+06
E_{33}^*	Young's modulus along matrix direction 3 (psi)	1.28E+06
ν_{12}^*	Poisson's ratio	0.342
ν_{13}^*	Poisson's ratio	0.342
ν_{23}^\dagger	Poisson's ratio	0.35
G_{12}^*	Shear modulus in 1-2 plane (psi)	7.80E+05
G_{13}^*	Shear modulus in 1-3 plane (psi)	7.80E+05
G_{23}^\ddagger	Shear modulus in 2-3 plane (psi)	431720
β^\S	Coefficient for stiffness proportional damping	1.00E-09
X_{1t}^*	Tensile failure stress in fiber direction (direction 1) (psi)	3.50E+05
X_{1c}^*	Compressive failure stress in fiber direction (direction 1) (psi)	1.67E+05
X_{2t}^*	Tensile failure stress in direction 2 (transverse to fiber direction) (psi)	9.41E+03
X_{2c}^{**}	Compressive failure stress in direction 2 (transverse to fiber direction) (psi)	3.55E+04
X_{3t}^*	Tensile failure stress in direction 3 (transverse to fiber direction) (psi)	9.41E+03
X_{3c}^{**}	Compressive failure stress in direction 3 (transverse to fiber direction) (psi)	3.55E+04
S_{12}^*	Shear strength in 1-2 plane (psi)	2.33E+04
S_{13}^*	Shear strength in 1-3 plane (psi)	2.33E+04
S_{23}	Shear strength in 2-3 plane (psi)	14000

* "Carbon – PEEK Composites." The Composite Materials Handbook MIL 17." Vol. 2. Baltimore, MD: ASTM International, 2002. Pg. 4-302 – 4-313

† D. R. Carlile, Leach, D. C., Moore, D. R., and Zahlan, N., "Mechanical Properties of the Carbon Fiber/PEEK Composite APC-2/AS-4 for Structural Applications," Advances in Thermoplastic Matrix Composite Materials, ASTM STP 1044, G. M. Newaz, Ed., American Society for Testing Materials, Philadelphia, 1989, pp. 199-212

‡ Downs, Keith. "Thermal Behavior and Thermal Stress analysis of Composite Laminates Containing High Thermal Conductivity Carbon Fibers," M. S. Thesis, Clemson University, Clemson, SC, 1995

§ ABAQUS Lecture Notes "Analysis of Composite Materials with ABAQUS."

** Klett, Lynn. "Long term Effects of Physiologic Saline on the Tensile Properties of Carbon Fiber/PEEK," M. S. Thesis, Clemson University, Clemson, SC, 1994

A second material, carbon epoxy, was tested to determine its effect on the ripper response. Table 2.2, below, lists the material properties of the carbon epoxy.

Table 2.2: Carbon Epoxy Material Properties

E_{11}^*	Young's modulus along fiber direction 1 (psi)	2.01E+07
E_{22}^*	Young's modulus along matrix direction 2 (psi)	1.46E+06
E_{33}^*	Young's modulus along matrix direction 3 (psi)	1.46E+06
ν_{12}^*	Poisson's ratio	0.26
ν_{13}^*	Poisson's ratio	0.41
ν_{23}^*	Poisson's ratio	0.26
G_{12}^*	Shear modulus in 1-2 plane (psi)	744000
G_{13}^*	Shear modulus in 1-3 plane (psi)	428000
G_{23}^*	Shear modulus in 2-3 plane (psi)	744000
β^\dagger	Coefficient for stiffness proportional damping	1.00E-09
X_{1t}^\ddagger	Tensile failure stress in fiber direction (direction 1) (psi)	150000
X_{1c}^\ddagger	Compressive failure stress in fiber direction (direction 1) (psi)	100000
X_{2t}^\ddagger	Tensile failure stress in direction 2 (transverse to fiber direction) (psi)	6000
X_{2c}^\ddagger	Compressive failure stress in direction 2 (transverse to fiber direction) (psi)	17000
X_{3t}^\ddagger	Tensile failure stress in direction 3 (transverse to fiber direction) (psi)	6000
X_{3c}^\ddagger	Compressive failure stress in direction 3 (transverse to fiber direction) (psi)	17000
S_{12}^\ddagger	Shear strength in 1-2 plane (psi)	10000
S_{13}^\ddagger	Shear strength in 1-3 plane (psi)	10000
S_{23}^\ddagger	Shear strength in 2-3 plane (psi)	6000

* Osborn, Christopher. "Feasibility of Integrating Advanced composite Materials into the Chassis of a Sports Car," M. S. Thesis, Clemson University, Clemson, SC, 2003

† ABAQUS Lecture Notes "Analysis of Composite Materials with ABAQUS."

‡ Jones, Robert M. Mechanics of Composite Materials. Philadelphia, PA : Taylor & Francis, 1999.

The plate to be ripped is constrained by the boundary conditions positioning the plate, as seen in Figure 2.3. It has a symmetric boundary condition along its entire back face, due to the symmetric stacking of the composites. An additional constraint is that the bottom face may not translate in the y- or z-direction. The final constraint is that the center point on the symmetric plane, shown in red in the figure below, cannot move in the x- or z-direction. This, coupled with the boundary conditions of the ripper, helps simplify the model and solution. The plate is shown with its “back” facing out.

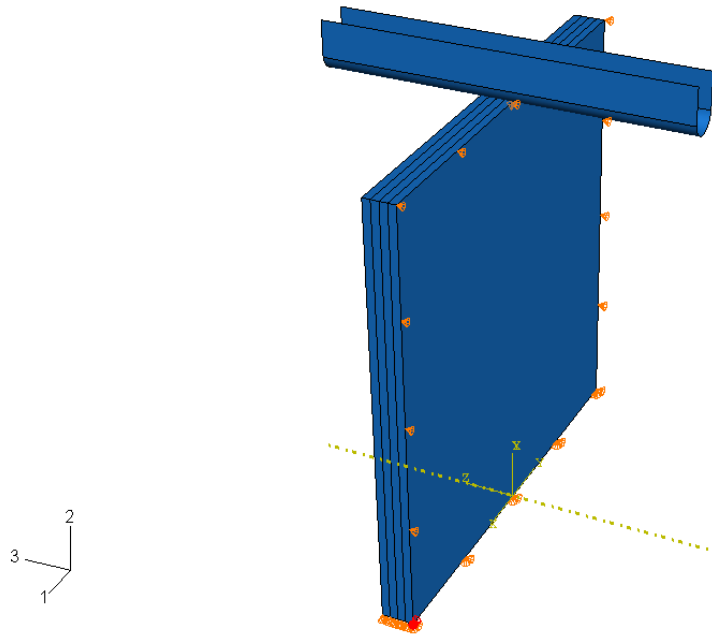


Figure 2.3: Plate Boundary Conditions

Friction

For both materials, a friction coefficient of 0.2²¹ was used for all cases. To verify the accuracy of the modeling, a friction verification case was conducted. The blade was allowed to move into the plate for 0.1 second at a speed of 5 inches per second and then move back

to its starting position. As elements within the model structurally fail, they were deleted, thus not contributing to the forces experienced by the ripper. If the model is accurate, the ripper force will go to zero. The results of this test, shown in Figure 2.4, indicate the model is accurate because the ripper force decrease to zero as soon as the blade leading edge ceases contact with the plate

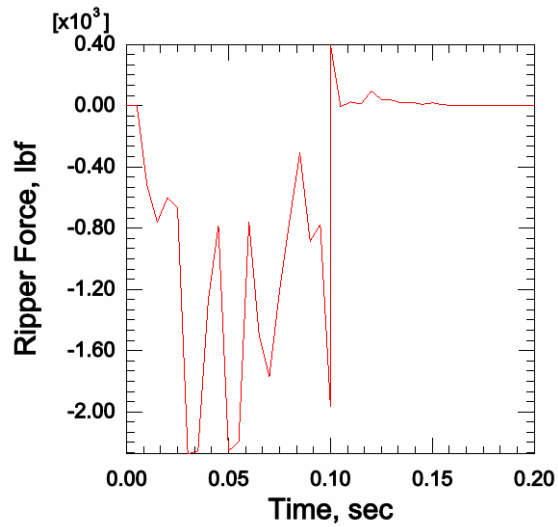


Figure 2.4: Friction Verification Case

It should be noted that while this case confirms that elements have been deleted from the model, the model is not accurate in the modeling of the ripper force while the ripper blade is moving upward to the starting position. This model does not account for damaged material interfering with the blade movement.

CHAPTER THREE

MODEL CREATION

The computer models developed for this research consisted of multiple unidirectional fiber lamina stacked in various orientations. A VUMAT provided by ABAQUS was used to model the material failure for a unidirectional fiber composite, thereby restricting the model to continuum elements. The element chosen, a C3D8R, is an eight-node brick with reduced integration and hourglass control. All cases were run using double precision, increasing the length of a floating point variable from 32 bits to 64 bits. This was recommended due to the large number of increments required for the analyses.

Mesh development

To determine the appropriate mesh density, multiple trials of meshes with general element sizes of 0.100, 0.075, 0.050, 0.040, 0.030, 0.025, and 0.023 inches were run. The size of the smallest mesh tested was partially determined by computer memory constraints. A total of eleven cases were analyzed, including a plane stress case and a comparative set for ply thickness versus repeated ply sequence for the $[-45/0/+45/90]_s$ sequence with both plates having the same total thickness. These cases were all prepared with the round ripper shape and carbon fiber/PEEK. The ply orientations used are listed below in Table 3.1:

Table 3.1: Ply Orientations

Ply Orientations	Ripper Shape	Material
$[-45/0/+45/90]_s$	Round	Carbon Fiber/PEEK
$[-45/0/+45/90]_s$	Sharp Point	Carbon Fiber/PEEK
$[-45/0/+45/90]_s$	Blunt	Carbon Fiber/PEEK
$[-45/0/+45/90]_s$	Round	Carbon Epoxy
$[0/90]_{2s}$	Round	Carbon Fiber/PEEK
$[-45/0/+45/0]_s$	Round	Carbon Fiber/PEEK
$[+30/-30]_{2s}$	Round	Carbon Fiber/PEEK
$[+60/-60]_{2s}$	Round	Carbon Fiber/PEEK

All 4-ply cases were examined at the same specified simulation time of 0.2 seconds at a constant speed to ensure that the ripping blade had moved the same distance into the plate and that element failure and removal had occurred. The 12-ply cases were examined at a specified simulation time of 0.16 seconds, determined by computing constraints. However, for comparison purposes the $[-45/0/+45/90]_{3s}$ case was continued to 0.2 seconds.

While all six stress components were considered when determining the appropriate mesh, the most emphasis was placed on σ_{22} , the stress in the direction of the ripper movement. The energy was calculated by integrating the reaction force from the ripper blade in the 2- direction over the ripper distance traveled and compared for all mesh densities. In view of the fact that energy absorption would be used for design comparison and viability, it was chosen for the convergence testing. In addition, it was discovered that when plate forces reached convergence, the energy had not yet converged to a single value. Figure 3.1, below, compares all mesh density cases energies as functions of the distance the ripper has moved.

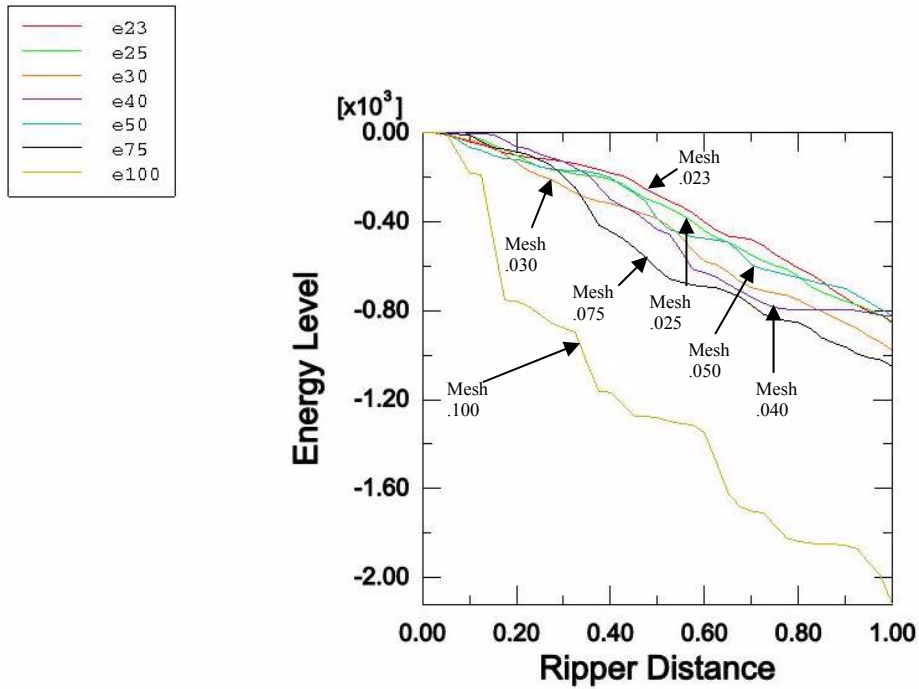


Figure 3.1: Mesh Density Case Energy Comparison

With the exception of the 0.100 case, the results for the other meshes seem to be clustering together to some degree. While, the 0.050 case appears close to the 0.025 case, this result seems to be a case of data aliasing. By removing the three least refined model results, a closer examination can be performed as shown in Figure 3.2 which compares the three finest mesh density cases, 0.040, 0.030, and 0.025.

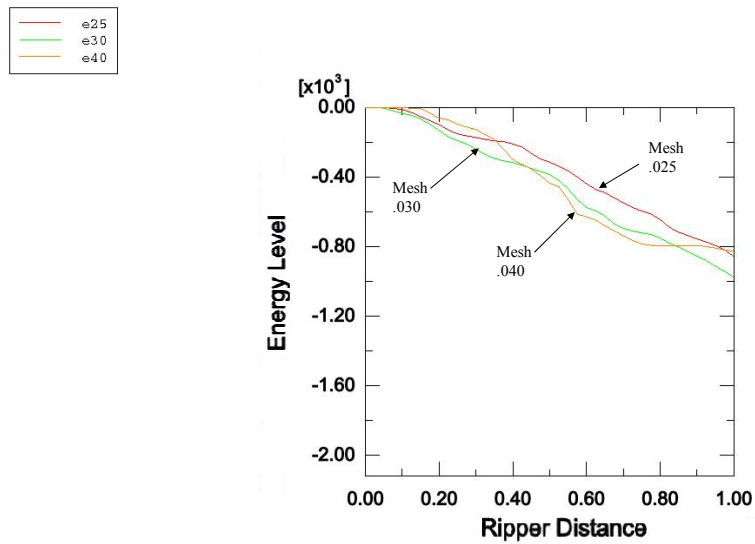


Figure 3.2: Energy Comparison for Mesh Densities 0.040, 0.030, and 0.025

Since the 0.030 mesh and the 0.025 mesh both closely follow a similar trend, one more refined mesh was created using a mesh density of 0.023 to determine if this trend toward convergence would continue with further refinement. A comparison of results of this most refined mesh with the results of the 0.025 mesh is shown in Figure 3.3, below.

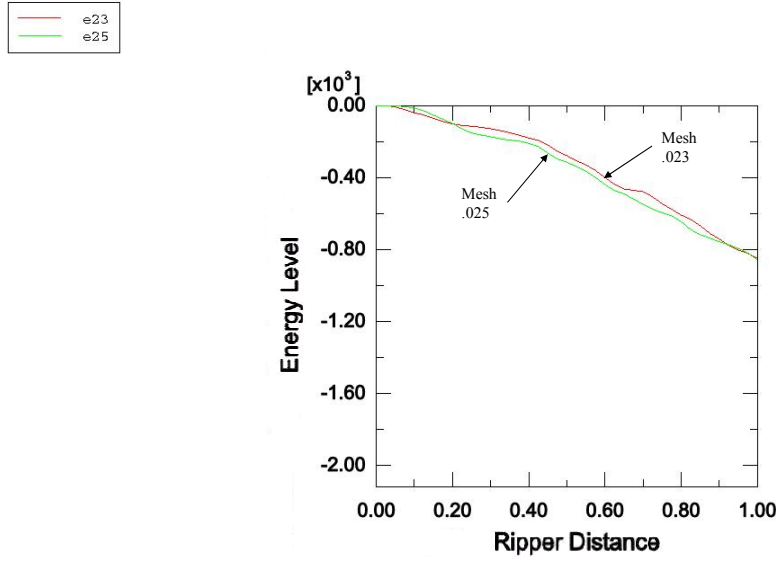


Figure 3.3: Energy Comparison for Mesh Densities 0.025 and 0.023

Given that the .023 mesh case energy absorption response closely follows the line form and values of the .025 mesh, it is judged that sufficient convergence has been reached and a mesh density of 0.025 was chosen for all cases analyzed in the remainder of this study.

Material Modeling

The unidirectional fiber composite was simulated using an orthotropic damage elasticity model. This stress-strain relationship for this composite is represented below in Equation(1).

$$\begin{pmatrix} \sigma_{11} \\ \sigma_{22} \\ \sigma_{33} \\ \sigma_{12} \\ \sigma_{23} \\ \sigma_{31} \end{pmatrix} = \begin{pmatrix} C_{11} & C_{12} & C_{13} & 0 & 0 & 0 \\ C_{12} & C_{22} & C_{23} & 0 & 0 & 0 \\ C_{13} & C_{23} & C_{33} & 0 & 0 & 0 \\ 0 & 0 & 0 & 2G_{12} & 0 & 0 \\ 0 & 0 & 0 & 0 & 2G_{23} & 0 \\ 0 & 0 & 0 & 0 & 0 & 2G_{31} \end{pmatrix} \begin{pmatrix} \epsilon_{11} \\ \epsilon_{22} \\ \epsilon_{33} \\ \epsilon_{12} \\ \epsilon_{23} \\ \epsilon_{31} \end{pmatrix} \quad (1)$$

Where the undamaged constants are:

$$C_{11}^0 = E_{11}^0 (1 - \nu_{23} \nu_{32}) \Gamma \quad (2)$$

$$C_{22}^0 = E_{22}^0 (1 - \nu_{13} \nu_{31}) \Gamma \quad (3)$$

$$C_{33}^0 = E_{33}^0 (1 - \nu_{12} \nu_{21}) \Gamma \quad (4)$$

$$C_{12}^0 = E_{11}^0 (\nu_{21} + \nu_{31} \nu_{23}) \Gamma \quad (5)$$

$$C_{23}^0 = E_{22}^0 (\nu_{32} + \nu_{12} \nu_{31}) \Gamma \quad (6)$$

$$C_{13}^0 = E_{11}^0 (\nu_{31} + \nu_{21} \nu_{32}) \Gamma \quad (7)$$

Where

$$\Gamma = 1 / (1 - \nu_{12} \nu_{21} - \nu_{23} \nu_{32} - \nu_{31} \nu_{13} - 2 \nu_{21} \nu_{32} \nu_{31}) \quad (8)$$

The global damage variables are represented by d_f , associated with the fiber failure mode, and d_m , for the matrix failure mode. These global damage variables are defined below in Equations 9 and 10, where d_{fc} , d_{ft} , d_{mc} , and d_{mt} are the variables associated with fiber compression and tension failure modes and the matrix compression and tension failure modes, respectively:

$$d_f = 1 - (1 - d_{ft})(1 - d_{fc}) \quad (9)$$

$$d_m = 1 - (1 - d_{mt})(1 - d_{mc}) \quad (10)$$

Incorporating Equations 9 and 10 with the undamaged constants in Equations 2 through 7 as well as with G_{12} , G_{13} , and G_{23} gives

$$C_{11} = (1 - d_f) C_{11}^0 \quad (11)$$

$$C_{22} = (1 - d_f)(1 - d_m) C_{22}^0 \quad (12)$$

$$C_{33} = (1 - d_f)(1 - d_m) C_{33}^0 \quad (13)$$

$$C_{12} = (1 - d_f)(1 - d_m) C_{12}^0 \quad (14)$$

$$C_{23} = (1 - d_f)(1 - d_m) C_{23}^0 \quad (15)$$

$$C_{13} = (1 - d_f)(1 - d_m) C_{13}^0 \quad (16)$$

$$G_{12} = (1 - d_f)(1 - s_{mt}d_{mt})(1 - s_{mc}d_{mc}) G_{12}^0 \quad (17)$$

$$G_{23} = (1 - d_f)(1 - s_{mt}d_{mt})(1 - s_{mc}d_{mc}) G_{23}^0 \quad (18)$$

$$G_{31} = (1 - d_f)(1 - s_{mt}d_{mt})(1 - s_{mc}d_{mc}) G_{31}^0 \quad (19)$$

The last three equations include the factors to aide in controlling the shear stiffness loss due to failure of the matrix in tension, s_{mt} , and in compression, s_{mc} . The factors were assumed to be 0.9 and 0.5, respectively.

Due to the complexities of modeling contact and the nonlinearities that can be involved, the model was developed using ABAQUS/Explicit rather than ABAQUS/Standard. While ABAQUS/Standard uses Newton's method, ABAQUS/Explicit uses an explicit central-difference time integration method²². It is referred to as explicit because the next state is calculated using positions, velocities, and accelerations from the current one. To create the model, system equations were put into matrix form. The local system equations are arranged into a matrix of the global system equations using node connectivity, simplifying the calculations and improving the efficiency of the computations. This creates a banded matrix, meaning that the equations are arranged

so that the all non-zero values lay along the diagonal. The explicit central-difference method requires extremely small increments to be used, the advantage being that the solution changes very little for each increment, meaning the errors remain even smaller. While a large number of increments are required, they tend to be relatively inexpensive computationally. In the flow chart of this algorithm seen in Figure 3.5, t is the time at a specified step, subscripted; M is the mass matrix discussed earlier; u , \dot{u} , and \ddot{u} , the displacements, velocities, and accelerations, respectively.

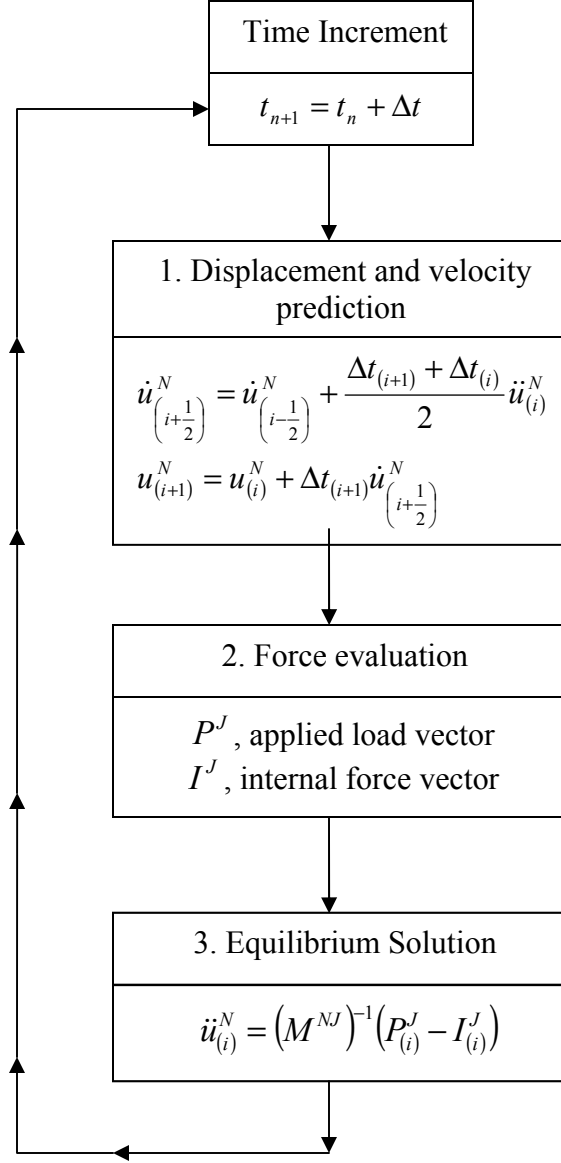


Figure 3.4: Explicit Central-Difference Time Integration^{23,24}

Because of the lamina orientation symmetry about the middle surface of the plate, the model was reduced to one half of a symmetric laminate. This simplification, which did not affect the data being collected, reduced the computation time of the simulations for the various composite lay-up configurations.

Contact Interaction Modeling

To simulate an accurate response from the carbon fiber, the contact characteristics for the entire assembly must be carefully defined and input, including all surfaces and interactions. This simulation was accomplished using ABAQUS/Explicit with contact pair definition because this explicit method allows for node-by-node enforcement of the contact without iteration²⁵.

In ABAQUS/Explicit, there are two ways of defining contact, either by general contact or contact pairs, both allowing for contact between rigid and deformable surfaces and contact of a body with itself. Defining contact between the model and itself allows for contact of pieces that fold in on the model, much like a crushed soda can has the possibility of creating holes in itself. However, since contact pairs allow for more detailed specifications, this method was chosen. Contact pairs require that two surfaces be chosen to contact. For the research reported here, the entire model was allowed to contact with itself, by defining all interior surfaces created by the mesh elements as one and the exterior as the second. Since contact in ABAQUS depends upon the specification of primary and secondary surfaces and since analytically rigid surfaces are by default allowed to be only primary contact surfaces, here, the ripper is always the primary surface and the plate including all its interior surfaces is the secondary surface. Primary surfaces force the deformation of the secondary surfaces.²⁵

In addition to defining contact pairs, contact properties such as friction, damping, slip, thermal conductance, and radiation, can also be defined. In this case, friction was defined as having a coefficient of 0.2²⁶.

Damage and Failure

To correctly model the material damage and failure in ABAQUS for a unidirectional composite fiber material an additional input file is needed. This file, a VUMAT, was provided by ABAQUS and is included in Appendix A. The material model was based on the theories of Hashin²⁷ and Puck²⁸.

Hashin's Failure Theory

Rather than looking at microstresses and failure due to a specific stress state, Hashin assumed the “existence of a three-dimensional failure criterion,” using average stresses or strains.²⁹ In doing so, he examined the works of Tsai³⁰, Hill³¹, Hoffman³², and Tsai and Wu³³. The Hashin failure criterion is quadratic in nature due to curve fitting not physical reasoning of material behavior. Since it is known that “all unidirectional fiber composites are transversely isotropic with respect to the fiber direction,” as a result of the random placement of fiber, the general form is

$$A_1 I_1 + B_1 I_1^2 + A_2 I_2 + B_2 I_2^2 + C_{12} I_1 I_2 + A_3 I_3 + A_4 I_4 = 1 \quad (20)$$

Where, due to the transverse isotropy of the material,

$$I_1 = \sigma_{11} \quad (21)$$

$$I_2 = \sigma_{22} + \sigma_{33} \quad (22)$$

$$I_3 = \sigma_{23}^2 - \sigma_{22}\sigma_{33} = \frac{1}{4}(\sigma_{22} - \sigma_{33})^2 + \sigma_{23}^2 \quad (23)$$

$$I_4 = \sigma_{12}^2 + \sigma_{13}^2 \quad (24)$$

To determine the constants, A_1 , A_2 , A_3 , A_4 , B_1 , B_2 , and C_{12} , various known stress states must be applied. After applying a pure transverse or axial shear loading individually, A_3 and A_4 are

shown in Equations (25) and (26), respectively, where τ_T is the transverse failure shear (1-2 plane) and τ_A is the axial failure shear (1-3 plane).

$$A_3 = \frac{1}{\tau_T^2} \quad (25)$$

$$A_4 = \frac{1}{\tau_A^2} \quad (26)$$

Since the fiber failure is all that is being examined with this loading, matrix failure modes may be eliminated. The fiber modes are dominated by the stresses σ_{11} , σ_{12} , and σ_{13} , allowing (20) to be simplified to

$$A_f \sigma_{11} + B_f \sigma_{11}^2 + \frac{1}{\tau_A^2} (\sigma_{12}^2 + \sigma_{13}^2) = 1 \quad (27)$$

Using information from a standard uniaxial tensile test, $\sigma_{11}^u = \sigma_A^+$, and using failure data for combined loading of σ_{11} and σ_{12} , the equation can be approximated for tensile fiber dominated failure within an elliptical failure envelope described by

$$\left(\frac{\sigma_{11}}{\sigma_A^+} \right)^2 + \frac{1}{\tau_A^2} (\sigma_{12}^2 + \sigma_{13}^2) = 1 \quad (28)$$

ABAQUS provides a tensile fiber dominated failure criterion

$$\left(\frac{\sigma_{11}}{X_{1t}} \right)^2 + \left(\frac{\sigma_{12}}{S_{12}} \right)^2 + \left(\frac{\sigma_{13}}{S_{13}} \right)^2 = 1 \quad (29)$$

Noting that $X_{1t} = \sigma_A^+$ and $\tau_A = S_{12}$, due to notation differences and since isotropy requires that $S_{12} = S_{13}$, the Equations (28) and (29) are the same.

Element Failure

When an element has reached failure as determined by the failure model, the element status is then changed from 1 to 0. At this point, the material point stresses are reduced to zero and it no longer contributes to the model stiffness. When all material points of an element have been reduced to zero, then the element is removed from the model mesh.

CHAPTER FOUR

RESULTS AND DISCUSSION

The variables examined here were the ply orientation, ply thickness, ripper shape, and material type. The laminates used to investigate ply orientation consisted of 8 ply layups stacked in ply orientations $[-45/0/+45/90]_S$, $[0/90]_{2S}$, $[-45/0/+45/0]_S$, $[+30/-30]_{2S}$, and $[+60/-60]_{2S}$. To examine the effect of ply thickness on the energy absorption and mechanism behavior, two cases were run: $[-45/0/+45/90]_{3S}$ at a thickness of 0.055" per ply, the same as in each of the previous cases, and $[-45/0/+45/90]_S$ at a thickness of 0.165" per ply, triple the thickness of the other cases. The ripper designs were rounded with a radius of 1/8", pointed to a sharp point with an angle approximately 90° , and a blunt end squared off with sharp 90° corners. The ripper width was held constant. The effects of two materials were also examined. All ply orientation and thickness cases were run using carbon fiber/PEEK. For comparison, a case of $[-45/0/+45/90]_S$ was run using carbon epoxy for the plate material.

To examine the extent of interlaminar effects seen in the results, a case considering only inplane failure was also run using the carbon fiber/PEEK for the plate material. To model this case, the out-of-plane material strengths were increased by six orders of magnitude, resulting in the elimination of these terms from the element material failure equations. Because of the potential application of this project as the front bumper of a racecar, the most important result of this study is the ripper reaction force versus displacement. Since the ripper moves at a constant velocity, its reaction force versus time has the same line form as the force versus displacement. This force can be integrated over

the time and then multiplied by the ripper velocity to obtain the energy absorption for helping to determine the plausibility and feasibility of the mechanism design.

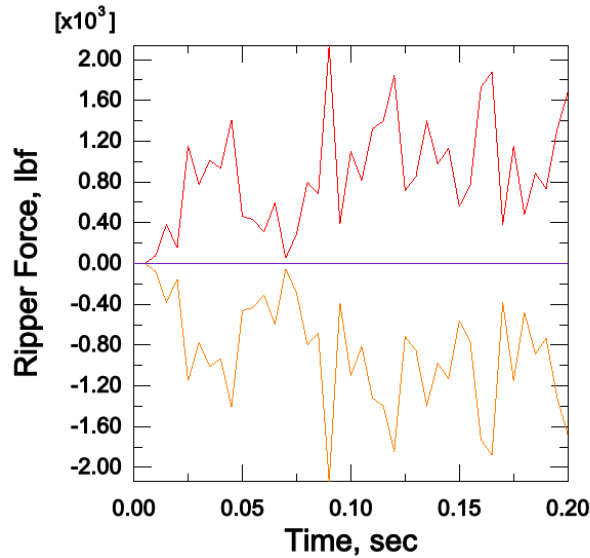


Figure 4.1: Complete Results Graph

Figure 4.1 shows the reaction force in all three directions and its magnitude. The magnitude of the reaction force is plotted in red, while the force in 2-direction is orange. The force in the 1- and 3- directions are both zero and therefore, appear as one purple line. For simplicity, all results plots will show only the 2-direction reaction force.

The sharp peaks and drops in this graph as well as in all other cases are due to plate cracking and element failure both of which are exemplified in Figures 4.2, 4.3, and 4.4 below. These figures illustrate element failure occurs in front of the ripper blade. In Figure 4.2, a failing element is colored blue due to its stress state and some elements just below the leading edge of the blade have already failed. For ease of viewing in Figures 4.3 and 4.4, these elements have been removed from the figures and are indicated by the empty spaces circled in white. The jerky movement of the blade through these empty spaces creates the

peaks and drops on the graph. As a result, the actual reaction force values are somewhere in between these two values.

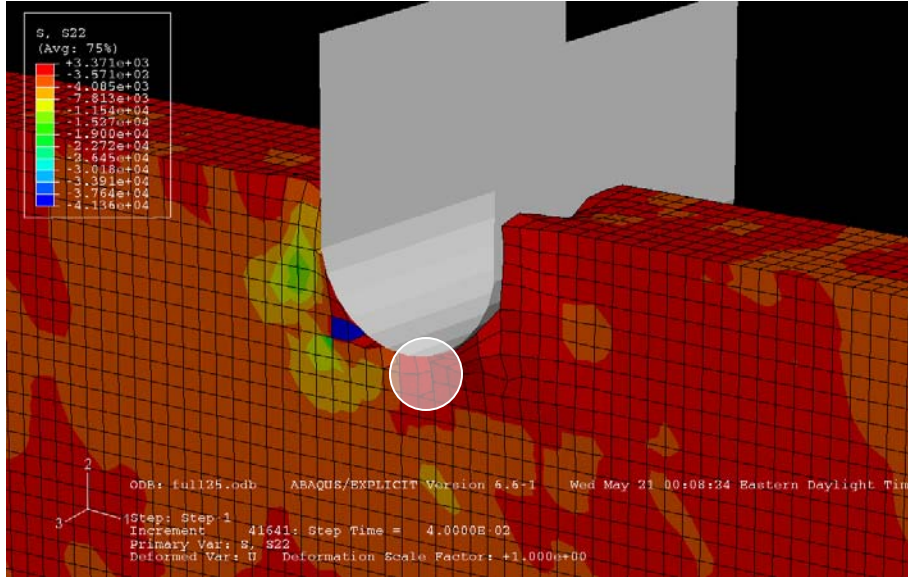


Figure 4.2: Element Failure on Plate

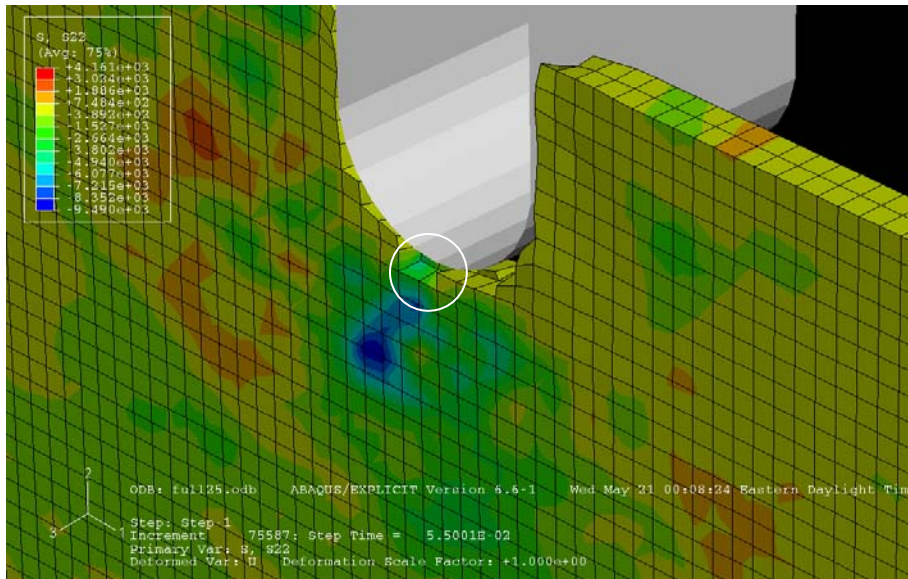


Figure 4.3: Element Failure on Zero-Degree Ply

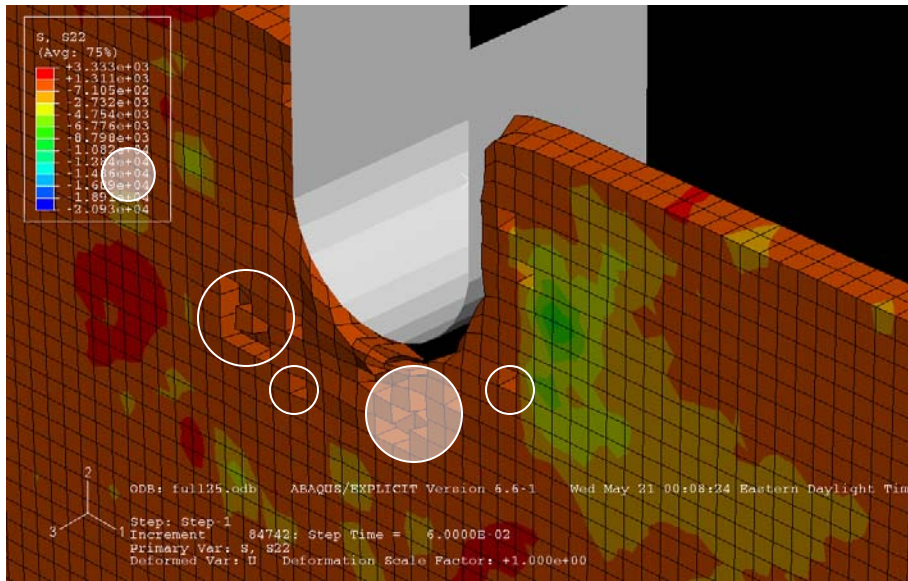


Figure 4.4: Element Failure on +45-Degree Ply

The following figures show the stress variations and plate deterioration as the ripper blade moves into the plate. The frames were captured at increments of 0.005 second; however, some frames were skipped for brevity. A complete set of output can be found in Appendix A.

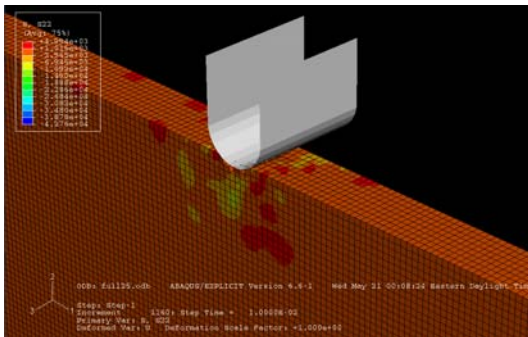


Figure 4.5: Stress Contour at 0.010s

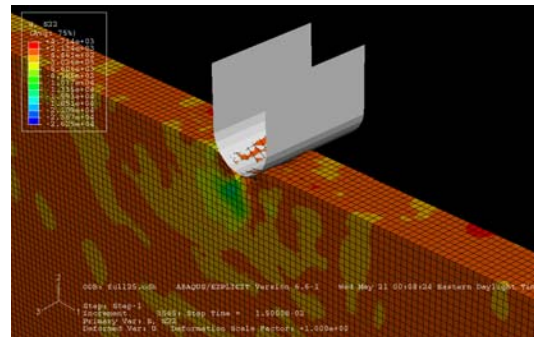


Figure 4.6: Stress Contour at 0.015s

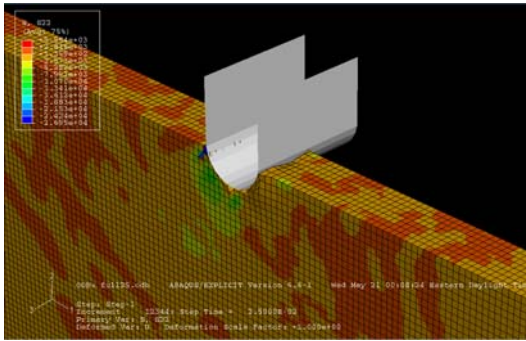


Figure 4.7: Stress Contour at 0.025s

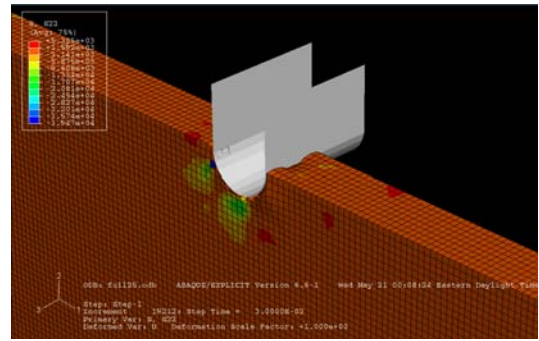


Figure 4.8: Stress Contour at 0.030s

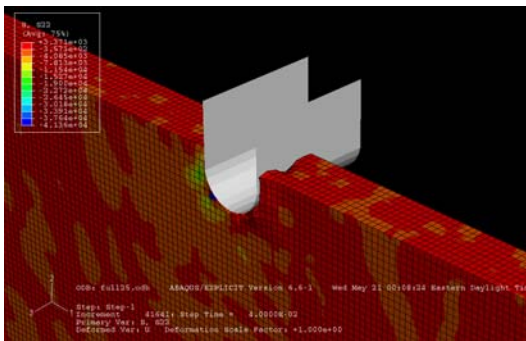


Figure 4.9: Stress Contour at 0.040s

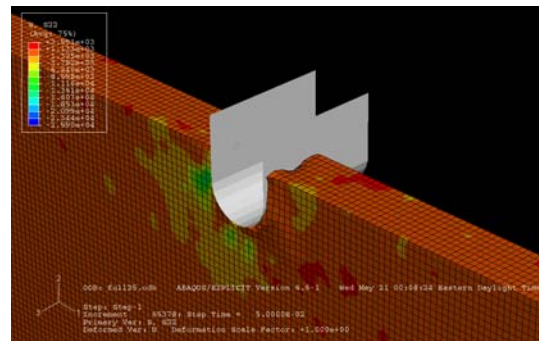


Figure 4.10: Stress Contour at 0.050s

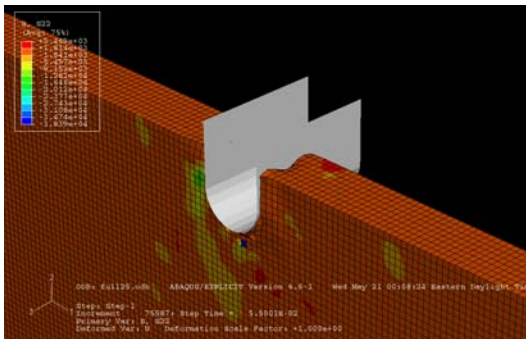


Figure 4.11: Stress Contour at 0.055s

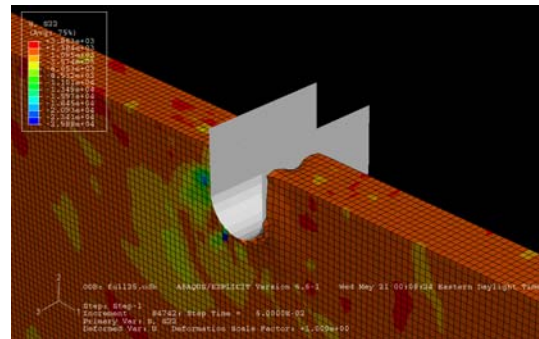


Figure 4.12: Stress Contour at 0.060s

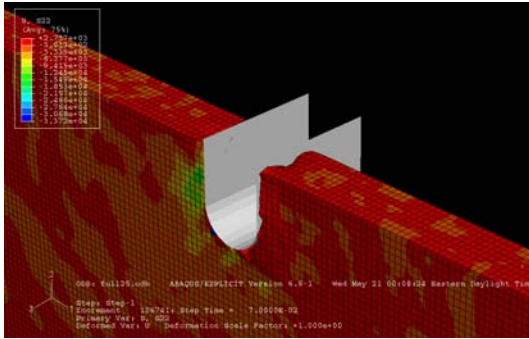


Figure 4.13: Stress Contour at 0.070s

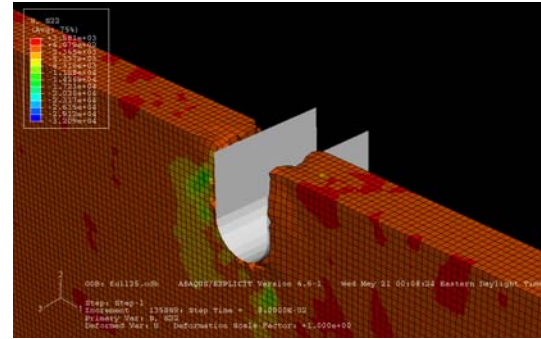


Figure 4.14: Stress Contour at 0.080s

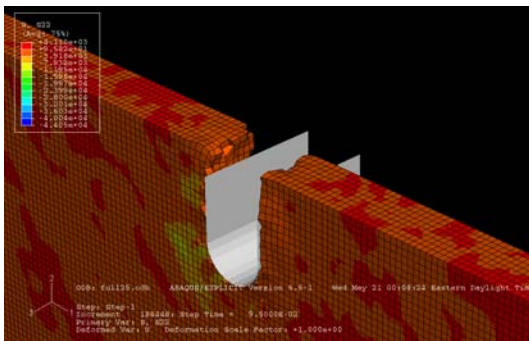


Figure 4.15: Stress Contour at 0.095s

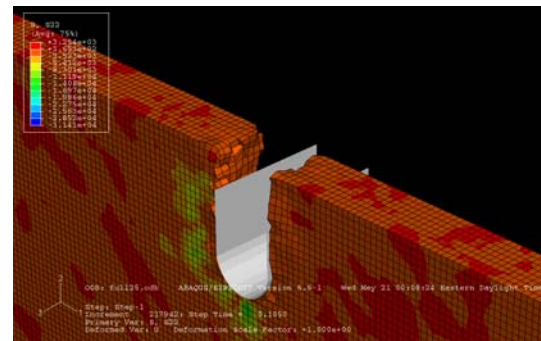


Figure 4.16: Stress Contour at 0.1050s

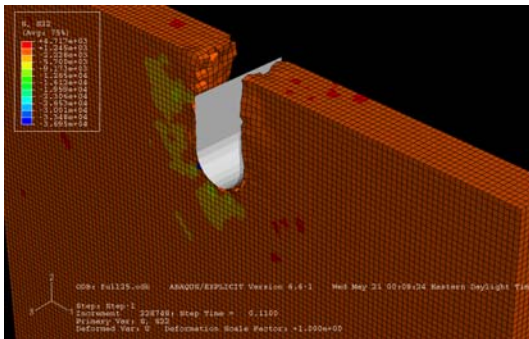


Figure 4.17: Stress Contour at 0.1100s

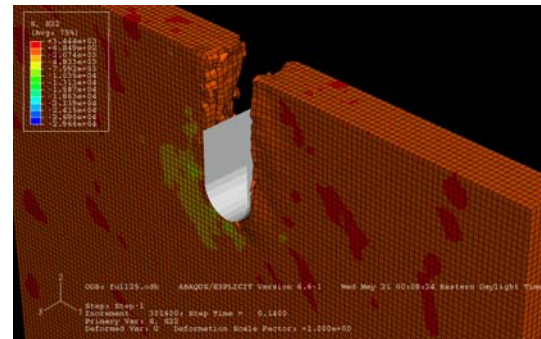


Figure 4.18: Stress Contour at 0.1400s

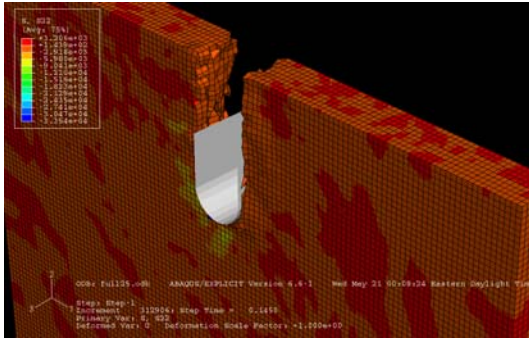


Figure 4.19: Stress Contour at 0.1450s

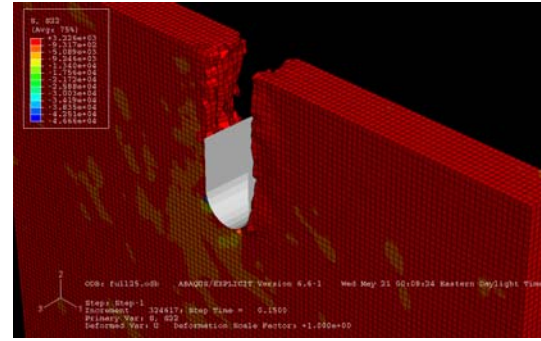


Figure 4.20: Stress Contour at 0.1500s

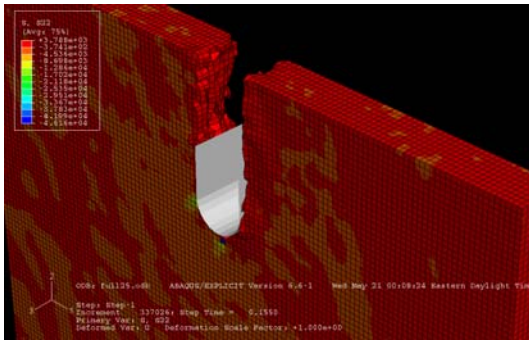


Figure 4.21: Stress Contour at 0.1550s

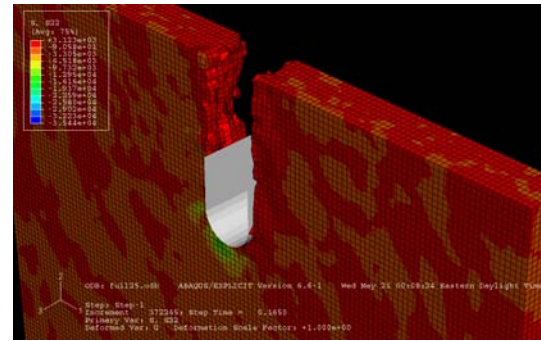


Figure 4.22: Stress Contour at 0.1650s

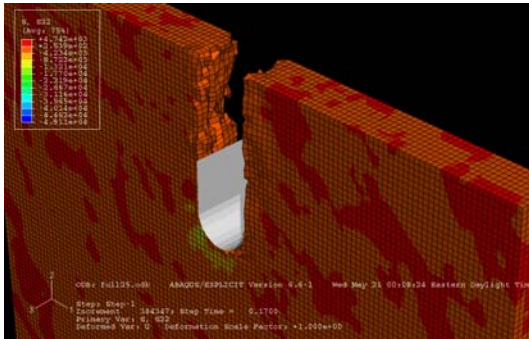


Figure 4.23: Stress Contour at 0.1700s

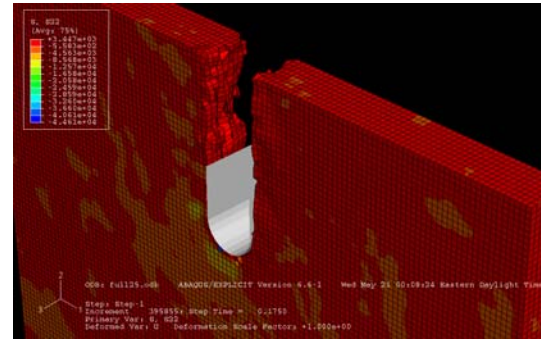


Figure 4.24: Stress Contour at 0.1750s

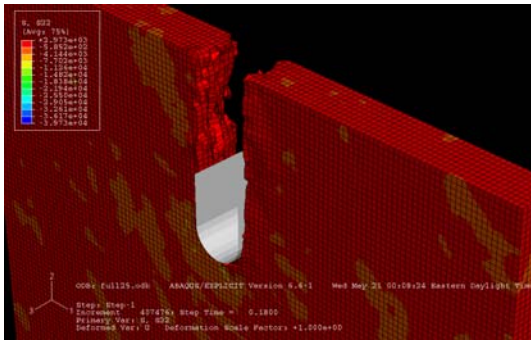


Figure 4.25: Stress Contour at 0.1800s

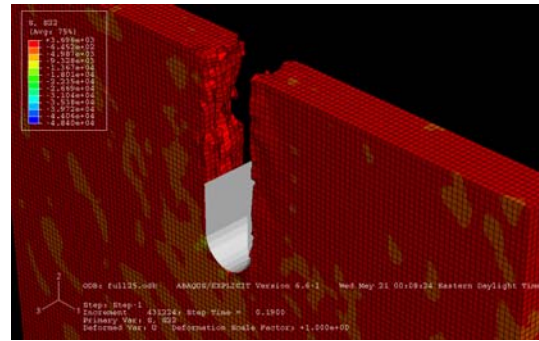


Figure 4.26: Stress Contour at 0.1900s

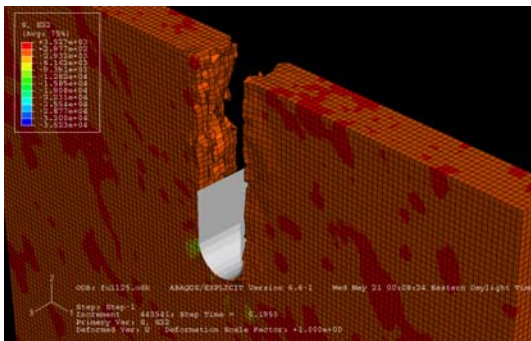


Figure 4.27: Stress Contour at 0.1950s

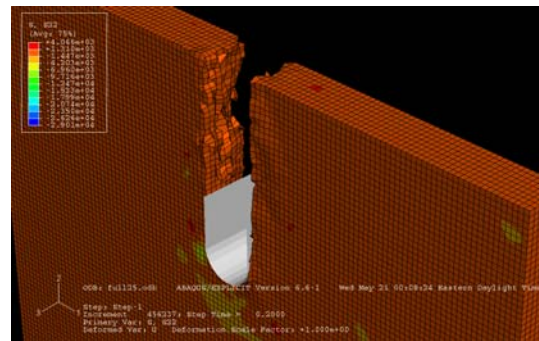


Figure 4.28: Stress Contour at 0.2000s

Since material choice can be a large consideration in design, two materials were chosen to investigate the magnitude of the effect of material variation on the ripper response. Figures 4.29 and 4.30 show the results for the carbon epoxy and carbon fiber/PEEK, respectively.

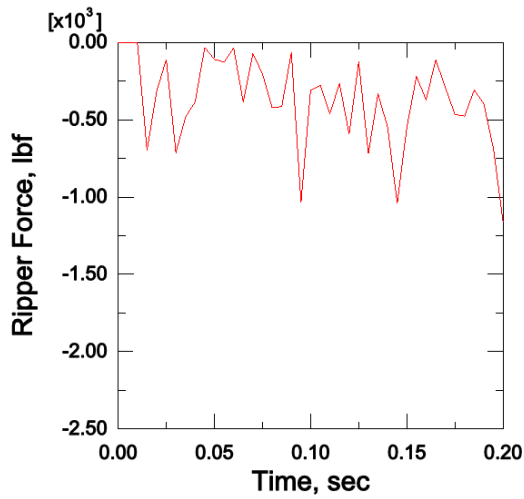


Figure 4.29: Carbon Epoxy Ply Reaction Force

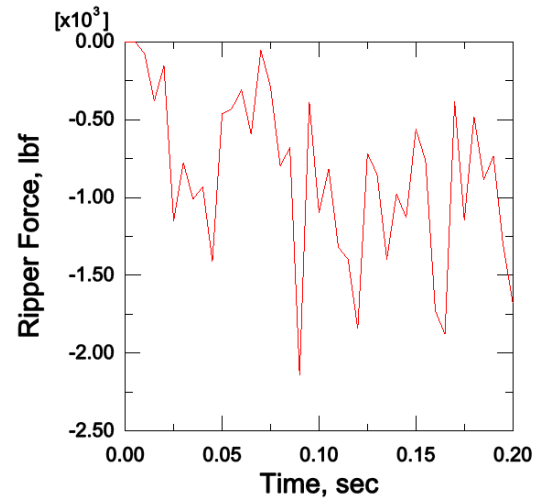


Figure 4.30: Carbon Fiber/PEEK Reaction Force

As these figures show the carbon/PEEK has a greater reaction force range than the carbon epoxy. This greater range results in a less smooth response but increases the energy absorbed by the mechanism. When the energy has been calculated for both materials, the carbon epoxy, 41.6785 J, absorbs only 43% as much energy as is absorbed by the carbon fiber/PEEK, 96.8578 J.

Next, the ripper shape was examined to determine the best shape for the proposed mechanism. Figures 4.31, 4.32, and 4.33 show the results for each ripper blade shape rounded, sharp, and blunt, respectively.

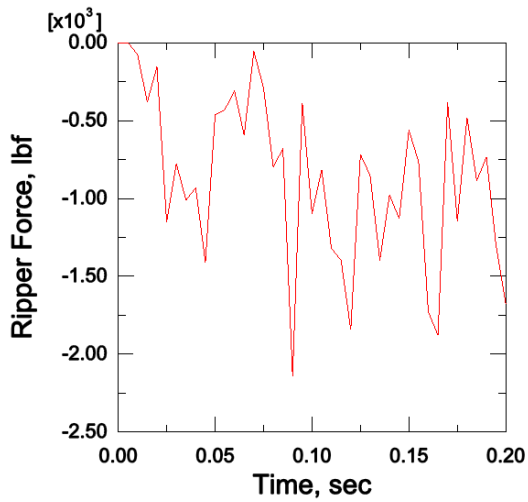


Figure 4.31: Rounded Ripper Reaction Force

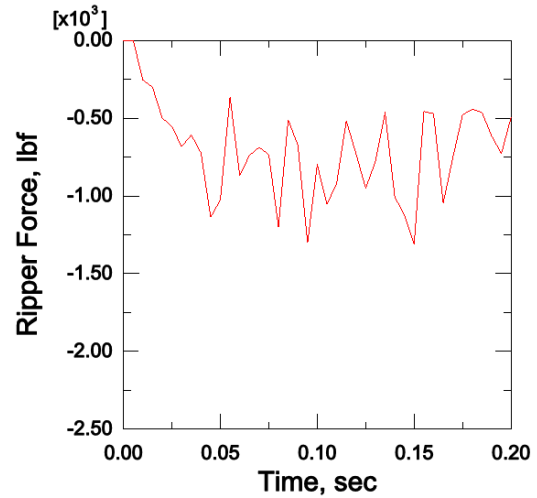


Figure 4.32: Sharp Ripper Reaction Force

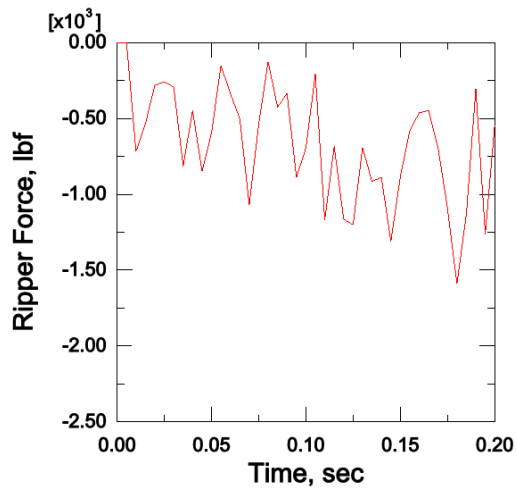


Figure 4.33: Blunt Ripper Reaction Force

As these figures show, the results for the three shapes are very different. As expected, the sharp blade has a smaller reaction range; however the rounded rather than the

blunt blade has the greatest reaction range. In order to aid in determining the appropriate blade shape, the energy absorbed must be analyzed. While approximately the same energy levels are absorbed by the sharp point and the blunt edge blades, the rounded tip absorbs more energy than the other two, an increase of 22% and 28%, respectively, suggesting that it is the most efficient of the three shapes.

To determine the best stacking sequence the plate ply orientation was studied. The figures, below, show the ripper reaction force results for the $[0/90]_{2S}$ ply orientation case:

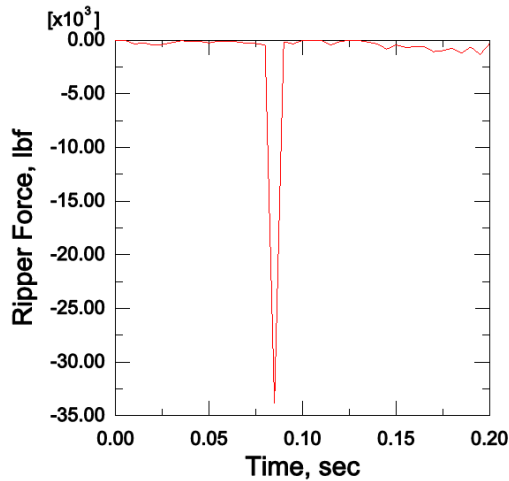


Figure 4.34: $[0/90]_{2S}$ Reaction Force Overall

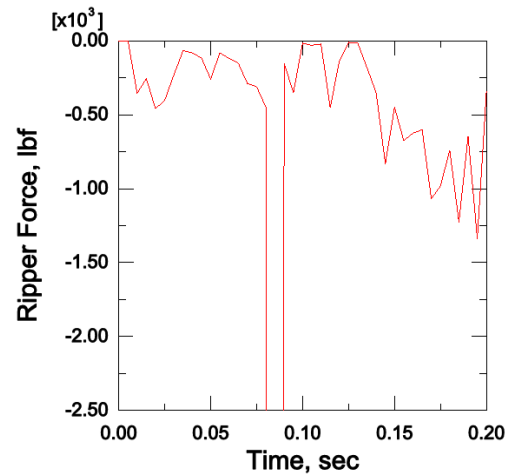


Figure 4.35: $[0/90]_{2S}$ Reaction Force Zoom In

It can easily be seen that the $[0/90]_{2S}$ case has a sharp downward force spike at 0.080 sec.

This is due to element failure in the zero degree plies before the 90 degree ply element failure. Figures 4.36 through 4.49 show the overall stress state for the composite plate and each of the plies at 0.075s, 0.080s, and 0.085s. It can easily be seen from these figures that the elements in the outer 0-degree ply fail in front of the ripper blade, while the 90-degree plies and second 0-degree ply have elements failing at the edge of the blade. This is due to the material properties of fiber strength versus matrix strength.

The second 0-degree ply has added strength because it is “sandwiched” between two stronger 90-degree plies.

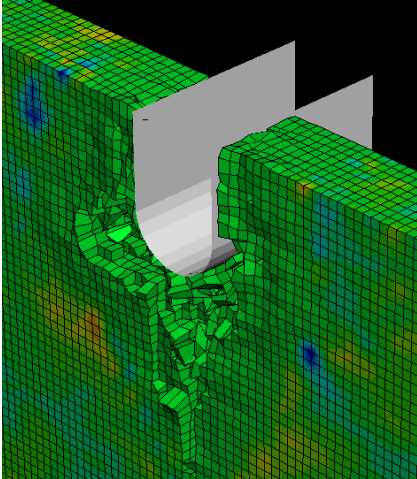


Figure 4.36: $[0/90]_{2s}$ Overall view at .075s

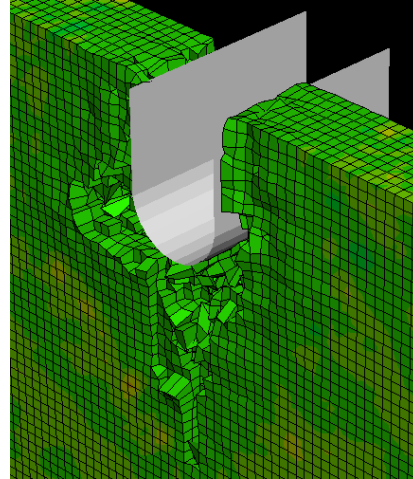


Figure 4.37: $[0/90]_{2s}$ Overall view at .080s

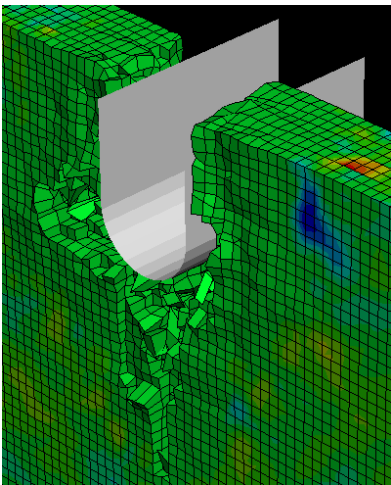


Figure 4.38: $[0/90]_{2s}$ Overall view at .085s

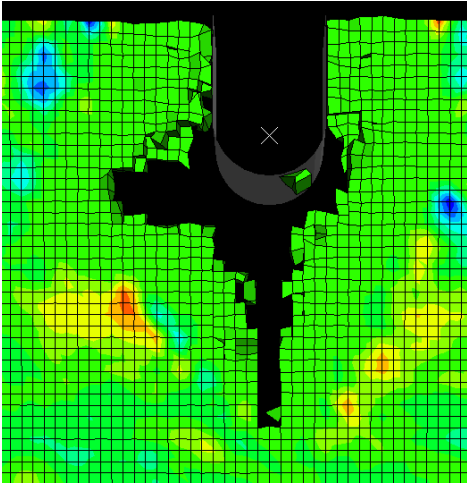


Figure 4.39: $[0/90]_{2s}$ Layer 1 view at .075s

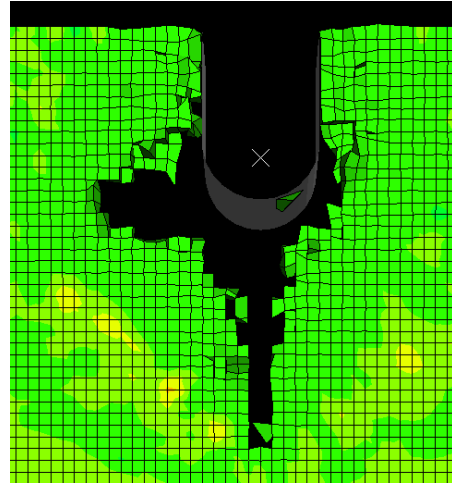


Figure 4.40: $[0/90]_{2s}$ Layer 1 view at .080s

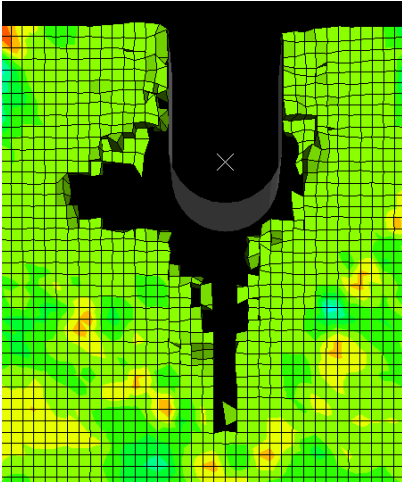


Figure 4.41: $[0/90]_{2s}$ Layer 1 view at .085s

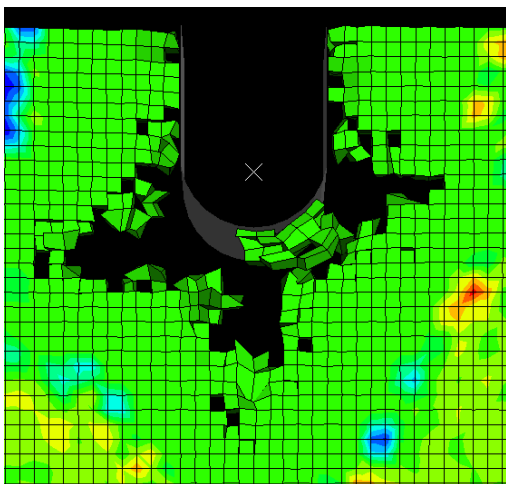


Figure 4.42: $[0/90]_{2s}$ Layer 2 view at .075s

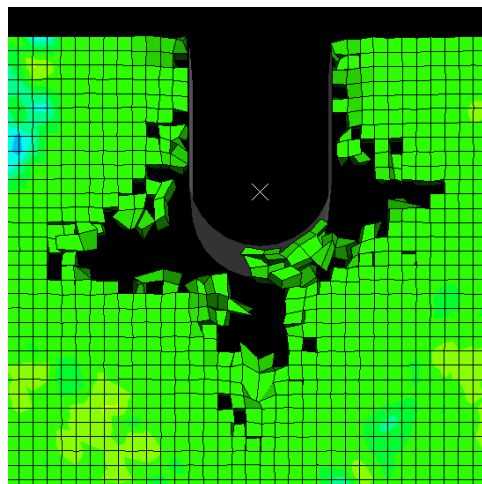


Figure 4.43: $[0/90]_{2s}$ Layer 2 view at .080s

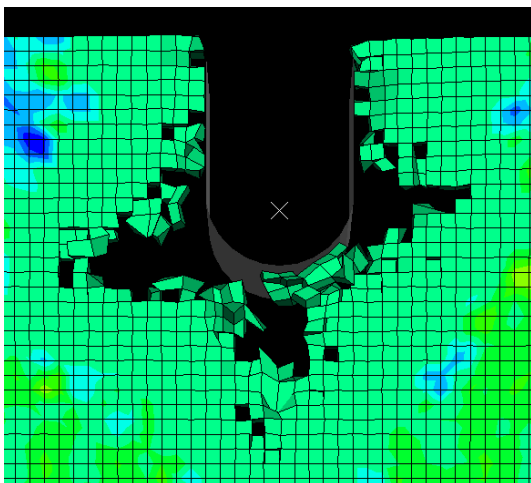


Figure 4.44: $[0/90]_{2s}$ Layer 2 view at .085s

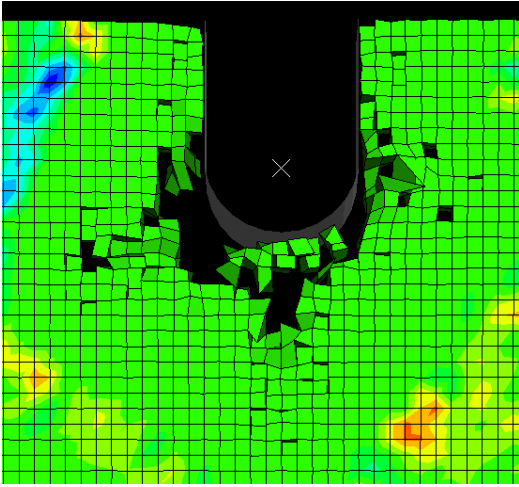


Figure 4.45: $[0/90]_{2s}$ Layer 3 view at .075s

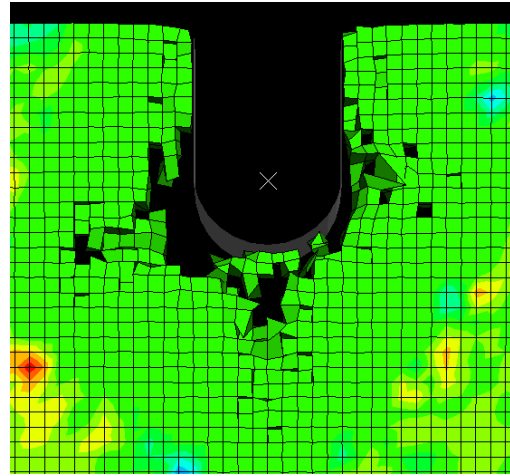


Figure 4.46: $[0/90]_{2s}$ Layer 3 view at .080s

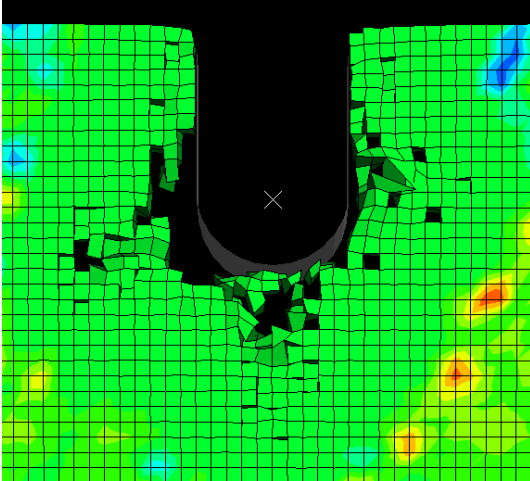


Figure 4.47: $[0/90]_{2s}$ Layer 3 view at .085s

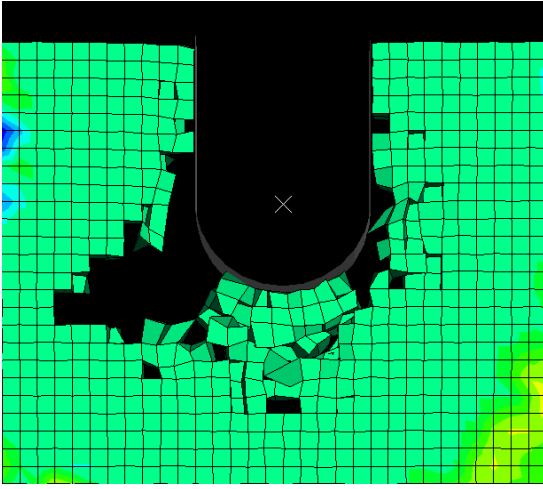


Figure 4.48: $[0/90]_{2s}$ Layer 4 view at .075s

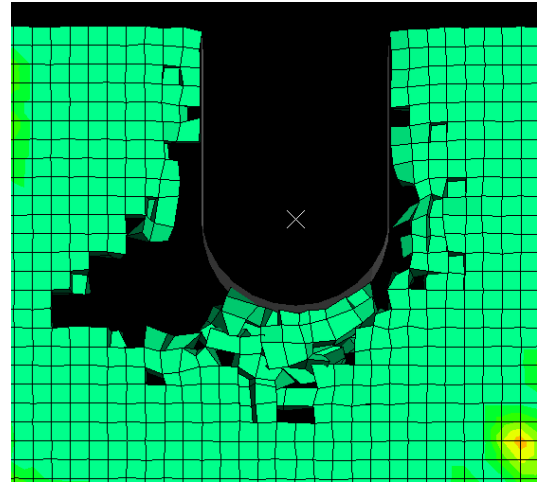


Figure 4.49: $[0/90]_{2s}$ Layer 4 view at .080s

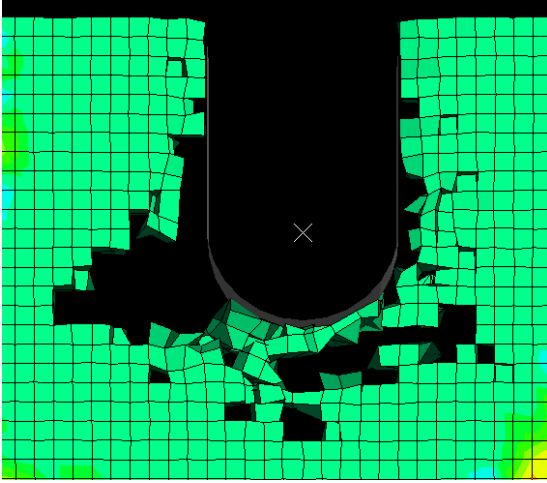


Figure 4.50: $[0/90]_{2s}$ Layer 4 view at .085s

With such a sharp force spike, this case may subject vehicle occupants to unsafe stopping due to excessive forces and force variations.

The other four ply orientation reaction force results are below in Figures 4.51, 4.52, 4.53, and 4.54 for ply orientations $[-45/0/+45/90]$, $[+30/-30]$, $[+60/-60]$, and $[-45/0/+45/90]$, respectively.

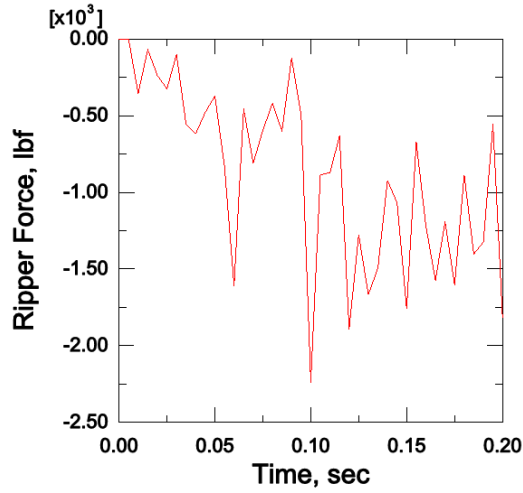


Figure 4.51: $[-45/0/+45/0]_s$ Reaction Force

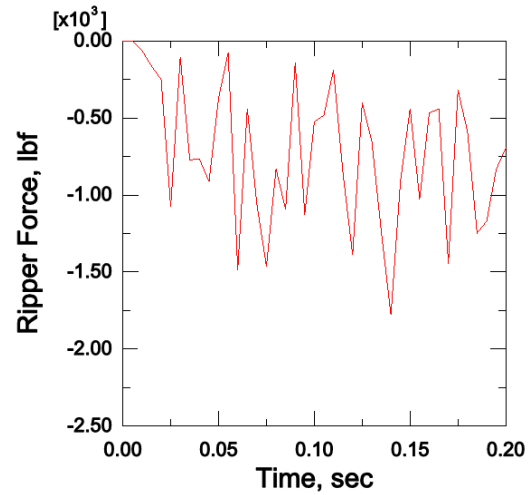


Figure 4.52: $[+30/-30]_{2s}$ Reaction Force

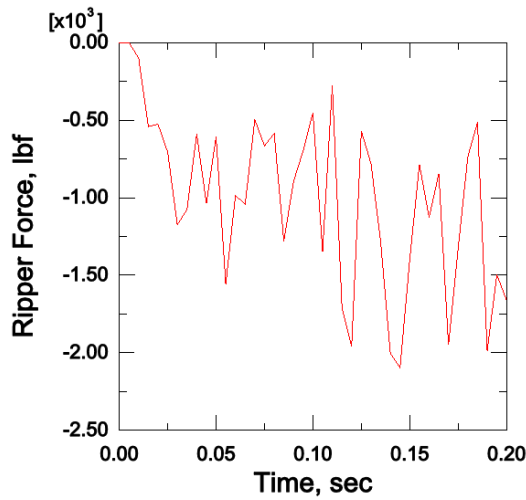


Figure 4.53: $[+60/-60]_{2s}$ Reaction Force

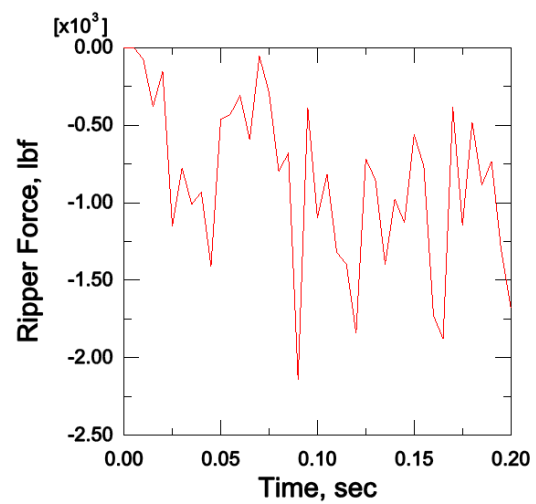


Figure 4.54: $[-45/0/+45/90]_s$ Reaction Force

The $[+60/-60]_{2s}$ and $[+30/-30]_{2s}$ force results have the least force variation. However, the $[-45/0/+45/0]_s$ and $[-45/0/+45/90]_s$ have fewer force peaks and very similar reactions. The energy absorbed by the $[-45/0/+45/0]_s$, 99.1419 J, and $[-45/0/+45/90]_s$, 96.8578 J, cases are within 5% of each other. This calculation also shows that the

$[+60/-60]_{2S}$, 113.097 J, case absorbs 17% more than either of the two 45-degree based orientations and 38% more than the $[+30/-30]_{2S}$, which absorbed the least amount of energy, 81.7854 J.

The final variable examined was ply thickness versus repeated plies using two cases of $[-45/0/+45/90]_{3S}$ and $[-45/0/+45/90]_S$. As noted, these cases were examined at a simulation time of 0.16 seconds, resulting in a ripper blade travel of 0.8 inches. Both involved the same overall plate thickness and the same percentage of plies in each orientation. The results can be seen in Figure 4.55 and 4.56 for the $[-45/0/+45/90]_{3S}$ and $[-45/0/+45/90]_S$, respectively.

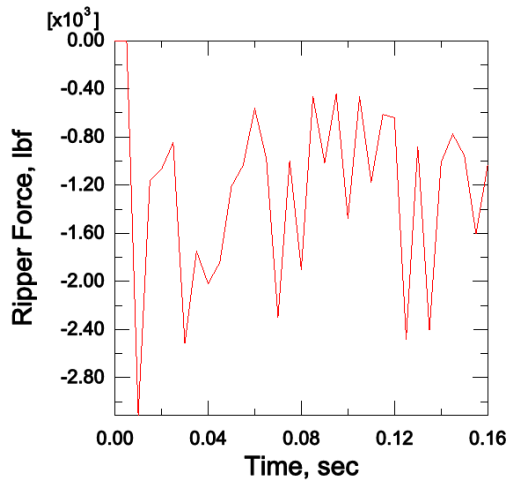


Figure 4.55: $[-45/0/+45/90]_S$ Thick Reaction Force

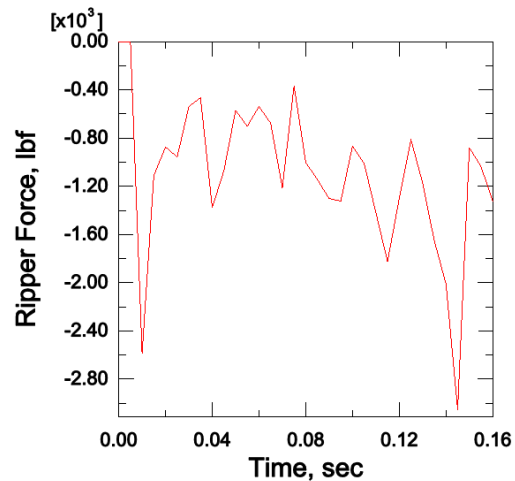


Figure 4.56: $[-45/0/+45/90]_{3S}$ Reaction Force

The $[-45/0/+45/90]_{3S}$ appears to provide a smoother response since its peaks and dips remain within a much smaller range than that of the $[-45/0/+45/90]_S$ case. Integrating the ripper blade reaction force over time and multiplying by the blade velocity gives the overall energy absorbed for each case. This calculation shows that despite the large peak in

the ripper reaction force in the $[-45/0/+45/90]_{3s}$ case, 100.32 J, the $[-45/0/+45/90]_s$, 113.603 J, absorbs approximately 13 % more energy.

To determine the effects of interlaminar stress and delamination, an in-plane failure model was prepared in which out-of-plane material strengths were increased resulting in their elimination from the failure equations. Therefore, only in-plane failure was allowed in the model. The ripping force results are shown below, with that of the 3D model.

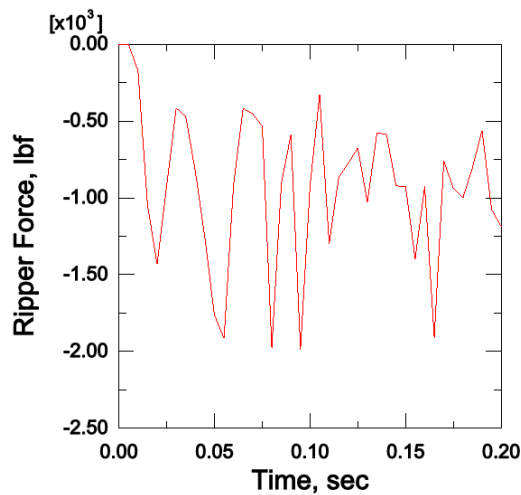


Figure 4.57: In-Plane Model Reaction Force

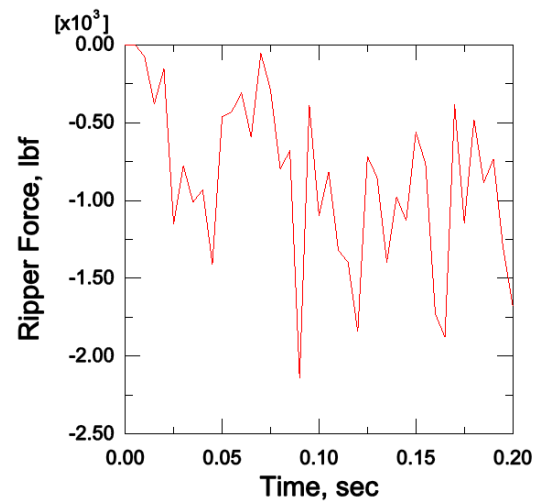


Figure 4.58: 3D Model Reaction Force

As expected, the in-plane failure model absorbs more energy than that of the 3D model because it does not allow for failure of the plate due to delamination and interlaminar stresses. Both delamination and interlaminar stresses weaken the plate and therefore reduce the energy levels absorbed by the plate. This confirms that the ABAQUS model was a complete 3D model, rather than a plane stress model. The in-plane failure model absorbed approximately 8% more energy than that of the full 3D model. This shows that the 3D model is a more conservative estimate of the actual energy absorption than the in-plane model.

CHAPTER FIVE

CONCLUSIONS

The two largest considerations in evaluating the system response are the smoothness of the response curve and the amount of energy absorbed by the system. The system energy absorption is the single most important output. In order to be a viable design for application in an automotive application, the mechanism will be required to absorb large amounts of energy. Therefore, the ripper blade and ply orientation with the highest energy levels are desired. The energy values obtained from the analyses are listed below in Table 5.1 and Table 5.2.

Table 5.1: Mechanism Energy Absorption

Ply Orientations	Ripper Shape	Material	Energy (J)
$[-45/0/+45/90]_s$	Round	Carbon Fiber/PEEK	96.8578
$[-45/0/+45/90]_s$	Sharp Point	Carbon Fiber/PEEK	79.7079
$[-45/0/+45/90]_s$	Blunt	Carbon Fiber/PEEK	75.7552
$[-45/0/+45/90]_s$	Round	Carbon Epoxy	41.6785
$[0/90]_{2s}$	Round	Carbon Fiber/PEEK	137.188
$[-45/0/+45/0]_s$	Round	Carbon Fiber/PEEK	99.1419
$[+30/-30]_{2s}$	Round	Carbon Fiber/PEEK	81.7854
$[+60/-60]_{2s}$	Round	Carbon Fiber/PEEK	113.097
$[-45/0/+45/90]_s$ In-plane case	Round	Carbon Fiber/PEEK	104.141
$[-45/0/+45/90]_{3s}$ at 0.2 sec	Round	Carbon Fiber/PEEK	140.238

Table 5.2: 12-ply Mechanism Energy Absorption at 0.16 sec

Ply Orientations	Ripper Shape	Material	Energy (J)
$[-45/0/+45/90]_s$ Thick ply case	Round	Carbon Fiber/PEEK	113.603
$[-45/0/+45/90]_{3s}$ at 0.16 sec	Round	Carbon Fiber/PEEK	100.32

It is easily determined that carbon fiber/PEEK provides much greater energy absorption than the carbon epoxy composite. With energy as the only consideration, the ideal design would be a round ripper blade with $[0/90]_{2S}$ ply orientation where the plies are made thicker rather than repeated for greater energy absorption. It is also easily concluded that the thicker plies function more efficiently than the repeated plies.

However, response curve smoothness should also be considered as the smoothness of the response curve relates to possible mechanism vibrations, the smoother the curve the fewer possible vibrations. The ripper shapes have been compared and highlighted in yellow in Table 5.3 below; the ply comparison is highlighted in green.

Table 5.3: Mechanism Response Curve Smoothness

Ply Orientations	Ripper Shape	Material	Smoothness Ranking
$[-45/0/+45/90]_S$	Round	Carbon Fiber/PEEK	3
$[-45/0/+45/90]_S$	Sharp Point	Carbon Fiber/PEEK	1
$[-45/0/+45/90]_S$	Blunt	Carbon Fiber/PEEK	2
$[0/90]_{2S}$	Round	Carbon Fiber/PEEK	5
$[-45/0/+45/0]_S$	Round	Carbon Fiber/PEEK	2
$[+30/-30]_{2S}$	Round	Carbon Fiber/PEEK	4
$[-45/0/+45/90]_S$	Round	Carbon Fiber/PEEK	1
$[+60/-60]_{2S}$	Round	Carbon Fiber/PEEK	3

By comparison, the sharp ripper blade created the smoothest response curve among the blade designs, while a ply orientation of $[-45/0/+45/90]_S$ produced the smoothest of the ply response curves. The best design would be a round ripper blade with a ply orientation $[+60/-60]_{2S}$ for the thinner plates. The $[+60/-60]_{2S}$ ply orientation was chosen over the $[0/90]_{2S}$ orientation due to the sharp drop in the $[0/90]_{2S}$ energy response. By tripling the overall plate thickness an increase of approximately 40% in energy absorption was achieved.

Therefore, thicker plates should be chosen where size and weight constraints allow. For thicker plates, a repeated ply sequence rather than thicker layers is preferred.

To put these results in perspective, a calculation using work-energy theorem was done to estimate the number of ripper blades required for varying speed impacts with a ripping distance of 6 inches. All calculations assumed a constant deceleration, and simultaneous ripper blade contact for all blades. For composite plate thickness of 0.44" due to the plate symmetry in the model, an impact of 10 mph for a 3000 lb vehicle into a stationary barrier would require 20 blades. An initial speed of 60 mph would require 720 blades. The thicker plate, 1.32 inches thick, would require 14 and 514 blades for 10 mph and 60 mph impacts, respectively. It can be seen that for high speed impacts, more design and research is needed.

APPENDICES

APPENDIX A

ABAQUS VUMAT

```
      subroutine vumat(  
c Read only -  
    1 nblock, ndir, nshr, nstatev, nfieldv, nprops, lanneal,  
    2 stepTime, totalTime, dt, cmname, coordMp, charLength,  
    3 props, density, strainInc, relSpinInc,  
    4 tempOld, stretchOld, defgradOld, fieldOld,  
    5 stressOld, stateOld, enerInternOld, enerInelasOld,  
    6 tempNew, stretchNew, defgradNew, fieldNew,  
c Write only -  
    7 stressNew, stateNew, enerInternNew, enerInelasNew )  
c  
    include 'vaba_param.inc'  
c  
c 3D Orthotropic Elasticity with Hashin 3d Failure criterion  
c  
c The state variables are stored as:  
c   state(*,1) = material point status  
c   state(*,2:7) = damping stresses  
c  
c User defined material properties are stored as  
c * First line:  
c   props(1) --> Young's modulus in 1-direction, E1  
c   props(2) --> Young's modulus in 2-direction, E2  
c   props(3) --> Young's modulus in 3-direction, E3  
c   props(4) --> Poisson's ratio, nu12  
c   props(5) --> Poisson's ratio, nu13  
c   props(6) --> Poisson's ratio, nu23  
c   props(7) --> Shear modulus, G12  
c   props(8) --> Shear modulus, G13  
c  
c * Second line:  
c   props(9) --> Shear modulus, G23  
c   props(10) --> beta damping parameter  
c   props(11) --> "not used"  
c   props(12) --> "not used"  
c   props(13) --> "not used"  
c   props(14) --> "not used"  
c   props(15) --> "not used"  
c   props(16) --> "not used"
```



```

c
c * Third line:
c  props(17) --> Ultimate tens stress in 1-direction, sigu1t
c  props(18) --> Ultimate comp stress in 1-direction, sigu1c
c  props(19) --> Ultimate tens stress in 2-direction, sigu2t
c  props(20) --> Ultimate comp stress in 2-direction, sigu2c
c  props(21) --> Ultimate tens stress in 2-direction, sigu3t
c  props(22) --> Ultimate comp stress in 2-direction, sigu3c
c  props(23) --> "not used"
c  props(24) --> "not used"
c
c * Fourth line:
c  props(25) --> Ultimate shear stress, sigu12
c  props(26) --> Ultimate shear stress, sigu13
c  props(27) --> Ultimate shear stress, sigu23
c  props(28) --> "not used"
c  props(29) --> "not used"
c  props(30) --> "not used"
c  props(31) --> "not used"
c  props(32) --> "not used"
c

dimension props(nprops), density(nblock),
1 coordMp(nblock,*),
2 charLength(*), strainInc(nblock,ndir+nshr),
3 relSpinInc(nblock,nshr), tempOld(nblock),
4 stretchOld(nblock,ndir+nshr), defgradOld(nblock,ndir+nshr+nshr),
5 fieldOld(nblock,nfieldv), stressOld(nblock,ndir+nshr),
6 stateOld(nblock,nstatev), enerInternOld(nblock),
7 enerInelasOld(nblock), tempNew(*),
8 stretchNew(nblock,ndir+nshr), defgradNew(nblock,ndir+nshr+nshr),
9 fieldNew(nblock,nfieldv), stressNew(nblock,ndir+nshr),
1 stateNew(nblock,nstatev),
2 enerInternNew(nblock), enerInelasNew(nblock)
*
character*80 cmname
*
parameter( zero = 0.d0, one = 1.d0, two = 2.d0, half = .5d0 )
*
parameter(
*   i_svd_DmgFiberT  = 1,
*   i_svd_DmgFiberC  = 2,
*   i_svd_DmgMatrixT = 3,
*   i_svd_DmgMatrixC = 4,
*   i_svd_statusMp   = 5,

```

```

*   i_svd_dampStress = 6,
c *   i_svd_dampStressXx = 6,
c *   i_svd_dampStressYy = 7,
c *   i_svd_dampStressZz = 8,
c *   i_svd_dampStressXy = 9,
c *   i_svd_dampStressYz = 10,
c *   i_svd_dampStressZx = 11,
*   i_svd_Strain   = 12,
c *   i_svd_StrainXx = 12,
c *   i_svd_StrainYy = 13,
c *   i_svd_StrainZz = 14,
c *   i_svd_StrainXy = 15,
c *   i_svd_StrainYz = 16,
c *   i_svd_StrainZx = 17,
*   n_svd_required = 17)
*
parameter(
*   i_s33_Xx = 1,
*   i_s33_Yy = 2,
*   i_s33_Zz = 3,
*   i_s33_Xy = 4,
*   i_s33_Yz = 5,
*   i_s33_Zx = 6)
*
* Structure of property array
parameter (
*   i_pro_E1   = 1,
*   i_pro_E2   = 2,
*   i_pro_E3   = 3,
*   i_pro_nu12 = 4,
*   i_pro_nu13 = 5,
*   i_pro_nu23 = 6,
*   i_pro_G12  = 7,
*   i_pro_G13  = 8,
*   i_pro_G23  = 9,
*
*   i_pro_beta = 10,
*
*   i_pro_sigu1t = 17,
*   i_pro_sigu1c = 18,
*   i_pro_sigu2t = 19,
*   i_pro_sigu2c = 20,
*   i_pro_sigu3t = 21,
*   i_pro_sigu3c = 22,
*   i_pro_sigu12 = 25,

```

```

*   i_pro_sigu13 = 26,
*   i_pro_sigu23 = 27 )
* Temporary arrays
  dimension eigen(maxblk*3)
*
* Read material properties
*
  E1 = props(i_pro_E1)
  E2 = props(i_pro_E2)
  E3 = props(i_pro_E3)
  xnu12 = props(i_pro_nu12)
  xnu13 = props(i_pro_nu13)
  xnu23 = props(i_pro_nu23)
  G12 = props(i_pro_G12)
  G13 = props(i_pro_G13)
  G23 = props(i_pro_G23)
*
  xnu21 = xnu12 * E2 / E1
  xnu31 = xnu13 * E3 / E1
  xnu32 = xnu23 * E3 / E2
*
*
* Compute terms of stiffness matrix
  gg = one / ( one - xnu12*xnu21 - xnu23*xnu32 - xnu31*xnu13
  *   - two*xnu21*xnu32*xnu13 )
  C11 = E1 * ( one - xnu23*xnu32 ) * gg
  C22 = E2 * ( one - xnu13*xnu31 ) * gg
  C33 = E3 * ( one - xnu12*xnu21 ) * gg
  C12 = E1 * ( xnu21 + xnu31*xnu23 ) * gg
  C13 = E1 * ( xnu31 + xnu21*xnu32 ) * gg
  C23 = E2 * ( xnu32 + xnu12*xnu31 ) * gg
*
  f1t = props(i_pro_sigu1t)
  f1c = props(i_pro_sigu1c)
  f2t = props(i_pro_sigu2t)
  f2c = props(i_pro_sigu2c)
  f3t = props(i_pro_sigu3t)
  f3c = props(i_pro_sigu3c)
  f12 = props(i_pro_sigu12)
  f13 = props(i_pro_sigu13)
  f23 = props(i_pro_sigu23)
*
  beta = props(i_pro_beta)
*
* Assume purely elastic material at the beginning of the analysis

```

```

*
  if ( totalTime .eq. zero ) then
    if ( nstatev .lt. n_svd_Required ) then
      call xplb_abqerr(-2,'Subroutine VUMAT requires the '//
*       'specification of %I state variables. Check the '//
*       'definition of *DEPVAR in the input file.',
*       n_svd_Required,zero,' ')
      call xplb_exit
    end if
    call OrthoEla3dExp ( nblock,
*     stateOld(1,i_svd_DmgFiberT),
*     stateOld(1,i_svd_DmgFiberC),
*     stateOld(1,i_svd_DmgMatrixT),
*     stateOld(1,i_svd_DmgMatrixC),
*     C11, C22, C33, C12, C23, C13, G12, G23, G13,
*     strainInc,
*     stressNew )
    return
  end if
*
* Update total elastic strain
  call strainUpdate ( nblock, strainInc,
*   stateOld(1,i_svd_strain), stateNew(1,i_svd_strain) )
*
* Stress update
  call OrthoEla3dExp ( nblock,
*   stateOld(1,i_svd_DmgFiberT),
*   stateOld(1,i_svd_DmgFiberC),
*   stateOld(1,i_svd_DmgMatrixT),
*   stateOld(1,i_svd_DmgMatrixC),
*   C11, C22, C33, C12, C23, C13, G12, G23, G13,
*   stateNew(1,i_svd_strain),
*   stressNew )
*
* Failure evaluation
*
  call copyr ( nblock,
*   stateOld(1,i_svd_DmgFiberT), stateNew(1,i_svd_DmgFiberT) )
  call copyr ( nblock,
*   stateOld(1,i_svd_DmgFiberC), stateNew(1,i_svd_DmgFiberC) )
  call copyr ( nblock,
*   stateOld(1,i_svd_DmgMatrixT), stateNew(1,i_svd_DmgMatrixT) )
  call copyr ( nblock,
*   stateOld(1,i_svd_DmgMatrixC), stateNew(1,i_svd_DmgMatrixC) )
  nDmg = 0

```

```

    call eig33Anal ( nblock, stretchNew, eigen )
    call Hashin3d ( nblock, nDmg,
*   f1t, f2t, f3t, f1c, f2c, f3c, f12, f23, f13,
*   stateNew(1,i_svd_DmgFiberT),
*   stateNew(1,i_svd_DmgFiberC),
*   stateNew(1,i_svd_DmgMatrixT),
*   stateNew(1,i_svd_DmgMatrixC),
*   stateNew(1,i_svd_statusMp),
*   stressNew, eigen )
*   -- Recompute stresses if new Damage is occurring
    if ( nDmg .gt. 0 ) then
        call OrthoEla3dExp ( nblock,
*   stateNew(1,i_svd_DmgFiberT),
*   stateNew(1,i_svd_DmgFiberC),
*   stateNew(1,i_svd_DmgMatrixT),
*   stateNew(1,i_svd_DmgMatrixC),
*   C11, C22, C33, C12, C23, C13, G12, G23, G13,
*   stateNew(1,i_svd_strain),
*   stressNew )
    end if
*
* Beta damping
    if ( beta .gt. zero ) then
        call betaDamping3d ( nblock,
*   beta, dt, strainInc,
*   stressOld, stressNew,
*   stateNew(1,i_svd_statusMp),
*   stateOld(1,i_svd_dampStress),
*   stateNew(1,i_svd_dampStress) )
    end if
*
* Integrate the internal specific energy (per unit mass)
*
    call EnergyInternal3d ( nblock, stressOld, stressNew,
*   strainInc, density, enerInternOld, enerInternNew )
*
    return
end

*****
*   OrthoEla3dExp: Orthotropic elasticity - 3d   *
*****
    subroutine OrthoEla3dExp ( nblock,
*   dmgFiberT, dmgFiberC, dmgMatrixT, dmgMatrixC,

```

```

*   C11, C22, C33, C12, C23, C13, G12, G23, G13,
*   strain, stress )
*
*   include 'vaba_param.inc'

* Orthotropic elasticity, 3D case -
*
*   parameter( zero = 0.d0, one = 1.d0, two = 2.d0)
*   parameter(
*     i_s33_Xx = 1,
*     i_s33_Yy = 2,
*     i_s33_Zz = 3,
*     i_s33_Xy = 4,
*     i_s33_Yz = 5,
*     i_s33_Zx = 6,
*     n_s33_Car = 6 )
*
*   dimension strain(nblock,n_s33_Car),
*     dmgFiberT(nblock), dmgFiberC(nblock),
*     dmgMatrixT(nblock), dmgMatrixC(nblock),
*     stress(nblock,n_s33_Car)
*   -- shear fraction in matrix tension and compression mode
*   parameter ( smt = 0.9d0, smc = 0.5d0 )
*
*   do k = 1, nblock
*     -- Compute damaged stiffness
*     dft = dmgFiberT(k)
*     dfc = dmgFiberC(k)
*     dmt = dmgMatrixT(k)
*     dmc = dmgMatrixC(k)
*     df = one - ( one - dft ) * ( one - dfc )
*
*     dC11 = ( one - df ) * C11
*     dC22 = ( one - df ) * ( one - dmt ) * ( one - dmc ) * C22
*     dC33 = ( one - df ) * ( one - dmt ) * ( one - dmc ) * C33
*     dC12 = ( one - df ) * ( one - dmt ) * ( one - dmc ) * C12
*     dC23 = ( one - df ) * ( one - dmt ) * ( one - dmc ) * C23
*     dC13 = ( one - df ) * ( one - dmt ) * ( one - dmc ) * C13
*     dG12 = ( one - df )
*       * ( one - smt*dmt ) * ( one - smc*dmc ) * G12
*     dG23 = ( one - df )
*       * ( one - smt*dmt ) * ( one - smc*dmc ) * G23
*     dG13 = ( one - df )
*       * ( one - smt*dmt ) * ( one - smc*dmc ) * G13
*   -- Stress update

```

```

        stress(k,i_s33_Xx) = dC11 * strain(k,i_s33_Xx)
*      + dC12 * strain(k,i_s33_Yy)
*      + dC13 * strain(k,i_s33_Zz)
        stress(k,i_s33_Yy) = dC12 * strain(k,i_s33_Xx)
*      + dC22 * strain(k,i_s33_Yy)
*      + dC23 * strain(k,i_s33_Zz)
        stress(k,i_s33_Zz) = dC13 * strain(k,i_s33_Xx)
*      + dC23 * strain(k,i_s33_Yy)
*      + dC33 * strain(k,i_s33_Zz)
        stress(k,i_s33_Xy) = two * dG12 * strain(k,i_s33_Xy)
        stress(k,i_s33_Yz) = two * dG23 * strain(k,i_s33_Yz)
        stress(k,i_s33_Zx) = two * dG13 * strain(k,i_s33_Zx)
    end do
*
    return
end

*****
* strainUpdate: Update total strain *
*****
subroutine strainUpdate ( nblock,
*   strainInc, strainOld, strainNew )
*
    include 'vaba_param.inc'
*
    parameter(
*      i_s33_Xx = 1,
*      i_s33_Yy = 2,
*      i_s33_Zz = 3,
*      i_s33_Xy = 4,
*      i_s33_Yz = 5,
*      i_s33_Zx = 6,
*      n_s33_Car = 6 )
*
    dimension strainInc(nblock,n_s33_Car),
*      strainOld(nblock,n_s33_Car),
*      strainNew(nblock,n_s33_Car)
*
    do k = 1, nblock
        strainNew(k,i_s33_Xx)= strainOld(k,i_s33_Xx)
*      + strainInc(k,i_s33_Xx)
        strainNew(k,i_s33_Yy)= strainOld(k,i_s33_Yy)
*      + strainInc(k,i_s33_Yy)
        strainNew(k,i_s33_Zz)= strainOld(k,i_s33_Zz)
*      + strainInc(k,i_s33_Zz)

```

```

      strainNew(k,i_s33_Xy)= strainOld(k,i_s33_Xy)
*          + strainInc(k,i_s33_Xy)
      strainNew(k,i_s33_Yz)= strainOld(k,i_s33_Yz)
*          + strainInc(k,i_s33_Yz)
      strainNew(k,i_s33_Zx)= strainOld(k,i_s33_Zx)
*          + strainInc(k,i_s33_Zx)
    end do
*
    return
  end

*****
* Hashin3d w/ Modified Puck: Evaluate Hashin 3d failure *
* criterion for fiber, Puck for matrix *
*****
      subroutine Hashin3d ( nblock, nDmg,
*       f1t, f2t, f3t, f1c, f2c, f3c, f12, f23, f13,
*       dmgFiberT, dmgFiberC, dmgMatrixT, dmgMatrixC,
*       statusMp, stress, eigen )
*
      include 'vaba_param.inc'

      parameter( zero = 0.d0, one = 1.d0, half = 0.5d0, three = 3.d0 )
      parameter(
*       i_s33_Xx = 1,
*       i_s33_Yy = 2,
*       i_s33_Zz = 3,
*       i_s33_Xy = 4,
*       i_s33_Yz = 5,
*       i_s33_Zx = 6,
*       n_s33_Car = 6 )
*
      parameter(i_v3d_X=1,i_v3d_Y=2,i_v3d_Z=3 )
      parameter(n_v3d_Car=3 )
*
      parameter ( eMax = 1.00d0, eMin = -0.8d0 )
*
      dimension  dmgFiberT(nblock), dmgFiberC(nblock),
*       dmgMatrixT(nblock), dmgMatrixC(nblock),
*       stress(nblock,n_s33_Car),
*       eigen(nblock,n_v3d_Car),
*       statusMp(nblock)
*
      f1tInv = zero

```



```

f2tInv = zero
f3tInv = zero
f1cInv = zero
f2cInv = zero
f3cInv = zero
f12Inv = zero
f23Inv = zero
f13Inv = zero
*
if ( f1t .gt. zero ) f1tInv = one / f1t
if ( f2t .gt. zero ) f2tInv = one / f2t
if ( f3t .gt. zero ) f3tInv = one / f3t
if ( f1c .gt. zero ) f1cInv = one / f1c
if ( f2c .gt. zero ) f2cInv = one / f2c
if ( f3c .gt. zero ) f3cInv = one / f3c
if ( f12 .gt. zero ) f12Inv = one / f12
if ( f23 .gt. zero ) f23Inv = one / f23
if ( f13 .gt. zero ) f13Inv = one / f13
*
do k = 1, nblock
  if ( statusMp(k) .eq. one ) then
*
    lFail = 0
*
    s11 = stress(k,i_s33_Xx)
    s22 = stress(k,i_s33_Yy)
    s33 = stress(k,i_s33_Zz)
    s12 = stress(k,i_s33_Xy)
    s23 = stress(k,i_s33_Yz)
    s13 = stress(k,i_s33_Zx)
*
*   Evaluate Fiber modes
    if ( s11 .gt. zero ) then
*   -- Tensile Fiber Mode
      rft = (s11*f1tInv)**2 + (s12*f12Inv)**2 + (s13*f13Inv)**2
      if ( rft .ge. one ) then
        lDmg = 1
        dmgFiberT(k) = one
      end if
    else if ( s11 .lt. zero ) then
*   -- Compressive Fiber Mode
      rfc = abs(s11) * f1cInv
      if ( rfc .ge. one ) then
        lDmg = 1
        dmgFiberC(k) = one

```

```

        end if
    end if
*
*   Evaluate Matrix Modes
    if ( ( s22 + s33 ) .gt. zero ) then
*   -- Tensile Matrix mode
        rmt = ( s11 * half * f1tInv )**2
*       + ( s22**2 * abs(f2tInv * f2cInv) )
*       + ( s12 * f12Inv )**2
*       + ( s22 * (f2tInv + f2cInv) )
        if ( rmt .ge. one ) then
            lDmg = 1
            dmgMatrixT(k) = one
        end if
        else if ( ( s22 + s33 ) .lt. zero ) then
*   -- Compressive Matrix Mode
            rmc = ( s11 * half * f1tInv )**2
*           + ( s22**2 * abs(f2tInv * f2cInv) )
*           + ( s12 * f12Inv )**2
*           + ( s22 * (f2tInv + f2cInv) )
            if ( rmc .ge. one ) then
                lDmg = 1
                dmgMatrixC(k) = one
            end if
        end if
*
        eigMax=max(eigen(k,i_v3d_X),eigen(k,i_v3d_Y),eigen(k,i_v3d_Z))
        eigMin=min(eigen(k,i_v3d_X),eigen(k,i_v3d_Y),eigen(k,i_v3d_Z))
        enomMax = eigMax - one
        enomMin = eigMin - one
*
        if ( enomMax .gt. eMax .or.
*           enomMin .lt. eMin .or.
*           dmgFiberT(k) .eq. one ) then
            statusMp(k) = zero
        end if
*
        nDmg = nDmk + lDmg
*
    end if
*
end do
*
return
end

```

APPENDIX B

POTENTIAL APPLICATION

The results of this study open the door to further research in this area. With crash energies for small vehicles at slow to nominal speeds reaching three orders of magnitude greater than the results seen here, more analysis of the ply thickness is required as well as the effect of multiple ripping blades.

Analysis of the complete device should also be done to determine whether it is feasible for vehicle application. The design should be examined for structural integrity during static loading and for impact loading, simulating a crash. Since this design uses materials with increased strength and stiffness to weight ratios, it should not add any weight to the vehicle. For ease of integration into existing systems, it can be easily installed with little or no modification to existing frame designs. The ripping mechanism can be adapted to fit the needs of platforms and conditions, and ideally it would be reusable after minor impacts, yet solid enough to hold up to daily driving or standard race conditions.

Based on the results of this study, the proposed design was virtually prototyped using Solid Works. The following six figures illustrate various views. Figure B-1 is the bottom view of the full bumper and ripping assembly. This view allows for the material removal slot in the bottom of the guide tube to be clearly seen. This system consists of a multi-material or composite material bumper, shown in gray; a ripping blade configuration, shown in green; and a guide tube, shown in blue. Each set of ripping blades sits in a guide tube located at the end of one of the parallel bumper supports. The material removal slot provides for directed removal of damaged material from the mechanism without jamming or clogging

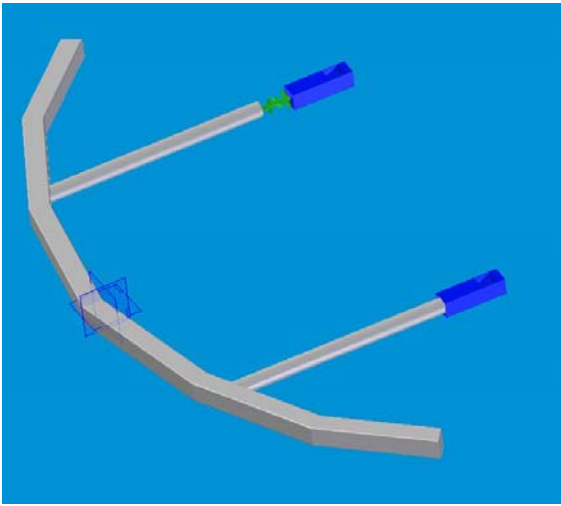


Figure B-1: Full Mechanism Assembly

In Figure B-2, a representative ripping blade set is shown in a guide tube. The blades are securely mounted in the guide tube to eliminate internal movement of the assembly. This mounting can be achieved by using either welds or pins on the blade pairs at both 0 and 90 degrees. While for passenger vehicles, one assembly configuration should be sufficient for each platform, however, for race vehicles, multiple assemblies may be required to accommodate varying race situations. In this case, multiple ripping assemblies could be prefabricated and interchanged, or blade configurations could be pinned in the guide tube as opposed to welded so that the tube would remain on the vehicle but the blades could be changed.

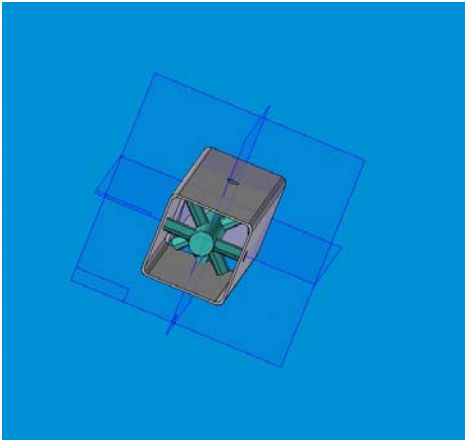


Figure B-2: Ripping Assembly

The ripping blade for the bumper design consists of blades spaced evenly around the axial center line either with or without a guiding cone as illustrated in Figures B-3 and B-4, respectively. Ripper blades are made of steel or another metallic material of similar or better suited properties.

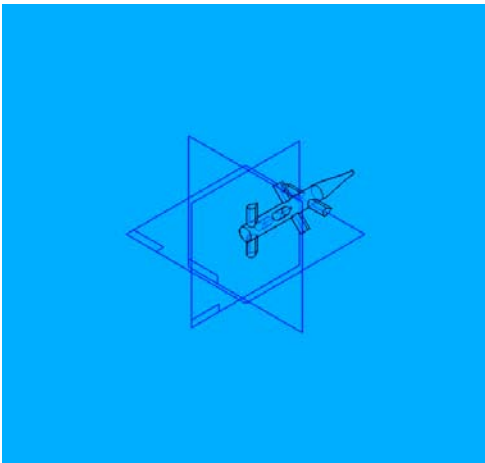


Figure B-3: Ripping blade with guide cone

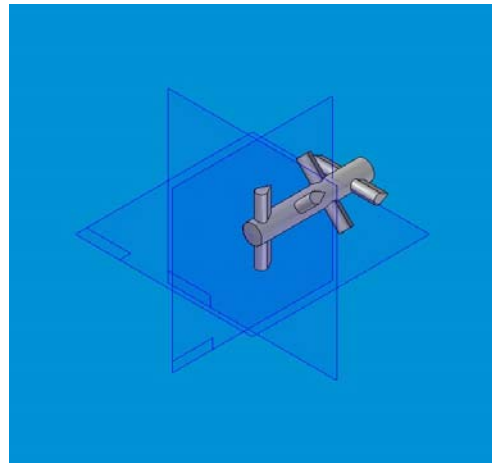


Figure B-4: Ripping Blade without
Guide

Cone

Two variations on the bumper design are shown in Figure B-5. The first bumper design, which requires minimal fitting to various manufacturer bumpers, complicates force distributions due to the angles involved, meaning further design is needed to ensure that the majority of manufacturer bumper designs would allow for this application. The second bumper design simplifies the force distributions by decreasing the number of angles in the structure. While it requires a lighter structure to create the support for the various manufacturer aesthetic bumper designs, it allows for greater variance in them. For either design, the front leading tube is constructed using either steel or composites, with the two parallel support tubes are made of a composite material, carbon fiber, probably.

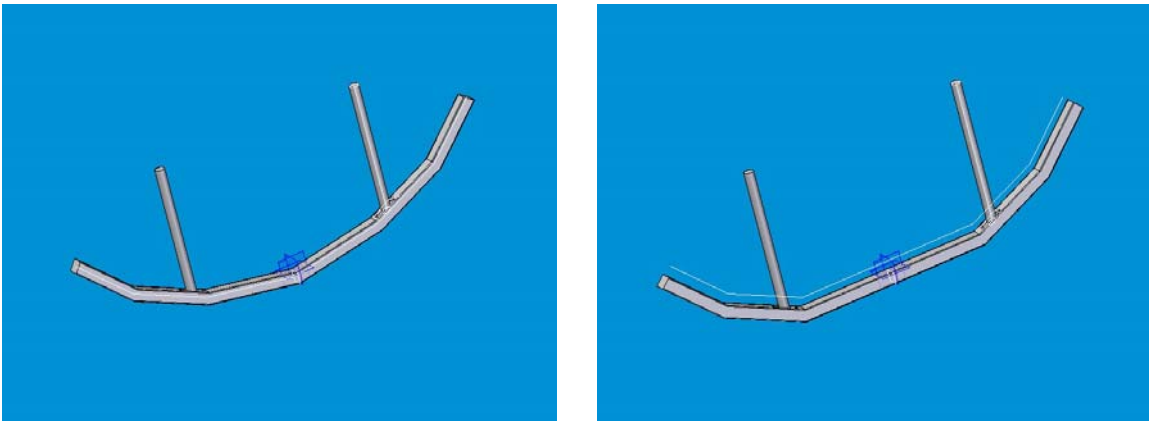


Figure B-5: Bumper Designs

The two guide tubes alternatives shown below in Figure B-6 mount to the existing roll cage replacing the existing bumper mount. The only difference between the designs is that the second design requires a spacing block to allow the funnel to aid in locating the support tube to prevent clogging or jamming. As with the ripping blade, the guide tube is constructed from steel.

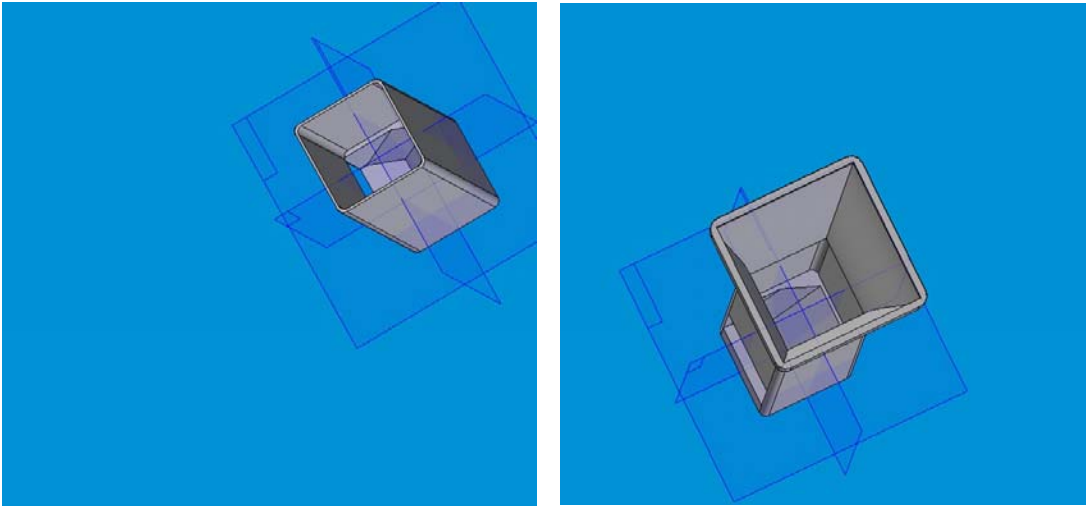


Figure B-6: Guide Tube Alternatives

The entire design requires further analysis before further prototyping can be done. The design will need analyzed as an impact on a half bumper to determine the blade orientation(s), number, and support tube composition.

REFERENCES

1. Van Dyke, Dave. "Fallen Hero: Earnhardt's death at Daytona leaves a permanent void." FOXSports.com 18 Feb 2001. 21 Oct 2007.
< <http://www2.foxsports.com/obits/earnhardt/vandy2.sml>>
2. "Kenny Irwin Is Killed During a Practice Run." The New York Times. 8 July 2000: D7
3. Siska, Ellen. "The SAFER barrier explained." 15 May 2007. 13 Nov 2007.
<<http://sports.espn.go.com/rpm/news/story?series=2&id=2863977>>
4. "NASCAR seeks safer racing through technology." Popular Mechanics. 2002 April. 05 Oct. 2006
<<http://www.popularmechanics.com/automotive/motorsports/1268996.html>>
5. "NASCAR Glossary." 5 Feb 2004. 13 Nov 2007.
<http://www.nascar.com/2002/kyn/nascar_101/02/02/glossary/>
6. Donovan, John. "Bumper-to-bumper racing leads to wild backstretch wreck." 2001 Feb 19. 21 Oct 2007
<http://sportsillustrated.cnn.com/motorsports/2001/daytona500/news/2001/02/18/wreck_side/>
7. McGinn, Daniel. "Tracking Safety." Newsweek. 16 Feb. 2004: 40
8. Juran, Ken. "Safer Racing: Lew Composites develops an energy-absorbing front bumper for NASCAR." Popular Mechanics. 2001 September. 05 Oct. 2006
<<http://www.popularmechanics.com/automotive/motorsports/1268996.html>>
9. Farley, Gary L. and Jones, Robert M. "Crushing characteristics of composite tubes with 'near-elliptical' cross sections" Journal of Composite Materials. Vol. 26, Jan. 1992, p 1741-1751
10. Farley, Gary L. "Effects of crushing speed on the energy-absorption capability of composite tubes." Journal of Composite Materials, Vol. 25, Oct. 1991, p 1314-1329
11. Albritton, James R. "Flared energy absorbing system and method." US Patent 7210874 01 May 2007
12. Albritton, James, R. "Energy Absorbing System for Fixed Roadside Hazards" European Patent 1112412 04 July 2001

13. Wallace, James. "Boeing unveils key new technology for Dreamliner." Seattle Post-Intelligencer. 2005 January 12. 10 Oct. 2006.
<http://seattlepi.nwsourc.com/business/207474_fuselage12.html>
14. Robbins, Tom. "The anti-jet lag plane." The Observer. 2006 July 23. 10 Oct. 2006
<<http://www.guardian.co.uk/travel/2006/jul/23/travelnews.theairlineindustry>>
15. Wallace, James. "Airbus has harsh words for Boeing's 7E7 'hype'." Seattle Post-Intelligencer. 2004 January 19. 4 Feb. 2007.
<http://seattlepi.nwsourc.com/business/207474_fuselage12.html>
16. ABAQUS v6.6. **SIMULIA**, Rising Sun Mills, 166 Valley Street, Providence, RI 02909
17. HKS (2006). "Getting Started with ABAQUS"
18. Downs, Keith. "Thermal Behavior and Thermal Stress analysis of Composite Laminates Containing High Thermal Conductivity Carbon Fibers," M. S. Thesis, Clemson University, Clemson, SC, 1995
19. D. R. Carlile, Leach, D. C., Moore, D. R., and Zahlan, N., "Mechanical Properties of the Carbon Fiber/PEEK Composite APC-2/AS-4 for Structural Applications," Advances in Thermoplastic Matrix Composite Materials, ASTM STP 1044, G. M. Newaz, Ed., American Society for Testing Materials, Philadelphia, 1989, pp. 199-212
20. Klett, Lynn. "Long term Effects of Physiologic Saline on the Tensile Properties of Carbon Fiber/PEEK," M. S. Thesis, Clemson University, Clemson, SC, 1994
21. "Quadrant EPP Ketron® PEEK CA30 (CM) Polyetheretherketone, 30% carbon fiber reinforced, compression molded." Quadrant Engineering Plastic Products. 4 Jan. 2007. <<http://quadrant.matweb.com/SpecificMaterial.asp?bassnum=P1SM17B>>
22. HKS (2006). "ABAQUS Theory Manual."
23. HKS (2006). "ABAQUS Theory Manual."
24. M. Geradin, Hogge, M. and Robert, G.. "Time Integration of Dynamic Equations." The Finite Element Handbook. Ed. H. Kardestuncer. New York: McGraw-Hill Book Company, 1987.
25. HKS (2006). "Getting Started with ABAQUS"

26. "Quadrant EPP Ketron® PEEK CA30 (CM) Polyetheretherketone, 30% carbon fiber reinforced, compression molded." Quadrant Engineering Plastic Products. 4 Jan. 2007. <<http://quadrant.matweb.com/SpecificMaterial.asp?bassnum=P1SM17B>>
27. Hashin, Z., "Failure Criteria for Unidirectional Fiber Composites," *Journal of Applied Mechanics*, Vol. 47, 1980, pp. 329-334.
28. Puck, A and Schürmann, H., "Failure Analysis of FRP Laminates By Means of Physically Based Phenomenological Models," *Composites Science and Technology*, Vol. 58, 1998, pp. 1045-1067.
29. Hashin, Z., "Failure Criteria for Unidirectional Fiber Composites," *Journal of Applied Mechanics*, Vol. 47, 1980, pp. 329-334.
30. Tsai, S. W., "Strength Characteristics of Composite Materials," NASA CR-224, 1965
31. Hill, R., "A Theory of the Yielding and Plastic Flow of Anisotropic Materials," *Proceedings of the Royal Society, Series A*, Vol. 193. 1948, p. 281
32. Hoffman, O., "The Brittle Strength of Orthotropic Materials," *Journal of Composite Materials*, Vol. 1, 1967 p. 200
33. Tsai, S. W., and Wu, E. M., "A General Theory of Strength for Anisotropic Materials," *Journal of Composite Materials*, Vol. 5, 1971, p. 448